

Surface mass balance and climate of the Last Glacial Maximum northern hemisphere ice sheets: simulations with CESM2.1

Sarah L. Bradley¹, Raymond Sellevold², Michele Petrini³, Miren Vizcaino², Sotiria Georgiou², Jiang Zhu⁴, Bette L. Otto-Bliesner⁴, and Marcus Lofverstrom⁵

¹Department of Geography, The University of Sheffield, Sheffield, UK

²Geosciences and remote sensing, Delft University of Technology, Delft, the Netherlands

³NORCE Norwegian Research Centre AS, Bjerknes Centre for Climate Research, Bergen, Norway

⁴Climate and Global Dynamics Laboratory, National Center for Atmospheric Research, Boulder, CO, USA

⁵Department of Geosciences, University of Arizona, Tuscon, AZ, USA

Correspondence: Sarah Bradley (s.l.bradley@sheffield.ac.uk), Miren Vizcaino (M.Vizcaino@tudelft.nl)

Abstract. The Last Glacial Maximum (LGM, from ~26 to 20 ka BP) was the most recent period with large ice sheets in Eurasia and North America. At that time, global temperatures were 5-7°C ~~colder~~lower than today, and sea level ~125 m lower. LGM simulations are useful to understand Earth System dynamics including climate-ice sheet interactions, and to evaluate and improve the models representing those. Here, we present two simulations of the Northern Hemisphere ice sheet climate and surface mass balance ~~with the (SMB) with the Community Earth System Model v2.1 (CESM2.1) using the Community Atmosphere Model v5~~ (CAM5) with prescribed ice sheets for two time periods that bracket the LGM period: 26 ka and 21 ka BP. CESM2.1 includes an explicit simulation of snow/firn compaction, albedo, refreezing, and direct coupling of the ice sheet surface energy fluxes with the atmosphere. The simulated mean ~~snowfall~~snow accumulation is lowest for the Greenland and Barents-Kara Sea Ice Sheets (GrIS, BKIS) and highest for British and Irish (BIIS) and Icelandic (IcIS) ice sheets. Melt rates are negligible for the dry BKIS and GrIS, and relatively large for the BIIS, ~~NAISC, SIS~~North American ice sheet complex (Laurentide, Cordillieran and Innuitian, NAISC), Scandinavian ice sheet (SIS) and IcIS, and are reduced by almost a third in the ~~colder~~ (lower temperature) 26 ka BP climate compared with 21 ka BP. The ~~surface mass balance (SMB)~~SMB is positive for the GrIS, BKIS, SIS and IcIS during the LGM (26 ka and 21 ka BP), and negative for the NAISC and BIIS. Relatively wide ablation areas are simulated along the southern (terrestrial), Pacific and Atlantic margins of the NAISC, across ~~all the majority~~ of the BIIS ~~surface~~, and along the terrestrial southern margin of the SIS. ~~For 26 ka BP climate the~~The integrated SMB substantially increases for the NAISC and BIIS in the 26 ka BP climate, but it does not reverse the negative sign. Summer incoming ~~solar radiation at the surface~~surface solar radiation is largest over the high interior of the NAISC and GrIS, and minimum over the BIIS and southern margin of NAISC. Summer net radiation is maximum over the ablation areas and minimum where the albedo is highest, namely in the interior of the GrIS, northern NAISC and all of the BKIS. Summer sensible and latent heat fluxes are highest over the ablation areas, positively contributing to melt energy. Refreezing is largest along the equilibrium line altitude for all ice sheets, and prevents 40-50 % of meltwater entering the ocean. ~~Our SMB results are in qualitative agreement with the climatic variability across the different northern hemisphere ice sheets.~~The large simulated melt for the NAISC suggests

potential biases in the climate simulation, ice sheet reconstruction, and/or highly non-equilibrated climate and ice sheet at the LGM time.

25 1 Introduction

Ice sheets play an important role in the Earth system through complex interactions with the atmospheric and oceanic circulation while simultaneously exerting a primary control on the global sea level (Fyke et al., 2018). The Greenland (GrIS) and Antarctic (AIS) ice sheets are expected to become the largest ~~contributer~~ contributors to future sea level rise. Projections of present-day ice sheet change and sea-level rise are primarily based on stand-alone ice sheet model simulations and/or regional climate modelling that provides robust representation of surface mass balance (SMB) change. However, neither of these modeling approaches include interactions between ice sheets and the global climate. Simulations of global climates with interactive ice sheets have been performed with intermediate complexity model (EMICS) or relatively low resolution AOGCMs including simplified SMB schemes (Ziemen et al., 2014; Quiquet et al., 2021). The coupling of global climate and ice sheet models is challenging (Muntjewerf et al., 2021), mainly due to the relatively coarse resolution of climate models compared to the required high resolution for an ice sheet model, and the large computational expense of running long climate simulations over multi-millennial timescales (Lofverstrom et al., 2020). Significant development has been made in the last decade, for instance, with the first realistic simulations of SMB with global models (~~Vizcaíno et al., 2013~~) (Vizcaíno et al., 2013; Smith et al., 2021), and more recently with the first realistic simulations of SMB and ice discharge within an Earth System Model with interactive ice sheets (Muntjewerf et al., 2020b; Sommers et al., 2021; Lofverstrom et al., 2020, 2022).

Here, we present ~~Community Earth System Model version 2.1 (CESM2.1)~~ simulations of the last glacial maximum (LGM) Northern Hemisphere ice sheets ~~with using the Community Earth System Model version 2.1 (CESM2.1). We use~~ a relatively high ~~resolution climate~~ resolution climate component ($\sim 1^\circ$) and an explicit calculation of ice sheet surface processes (melt energy fluxes, snow/ice compaction, albedo and refreezing evolution (Lawrence et al., 2019; Sellevold et al., 2019)). The LGM extended from 26 ka to 20/19 ka BP (Clark et al., 2009) and historically 21 ka BP has been used as the representative time period (Mix et al., 2001; Kageyama et al., 2017). During this 6 ka interval, atmospheric trace gases and ice core temperature records are relatively stable (see Fig. 1 ~~in~~ Ivanovic et al. (2016)), but the ~~solar insolation signal~~ insolation is steadily increasing and the timing of the local LGM of the continental ice sheets was highly asynchronous. For example, the North American ice sheet complex (NAISC, (Laurentide, Cordilleran and Innuitian)) is inferred to have reached its maximum extent at 25 ka BP. However, as the recent review by Dalton et al. (2022) highlights, regionally the LGM was asynchronous, earlier (ca. 27 ka BP) in the offshore region of western Canada, and later (ca. 18 ka BP) in the west. The Scandinavian (SIS) and Barents-Kara ice sheets (BKIS) coalesced and reached their maximum at 24 ka BP (Hughes et al., 2016) whereas the British and Irish and North sea ice sheet (BIIS) reached a maximum extent at 23 ka BP with rapid deglaciation initiated at 22 ka BP (Clark et al., 2022).

As previous studies have shown, modelling the LGM and maintaining a maximum glacial extent for both the NAISC and SIS has been problematic (~~Ziemen et al., 2014; Quiquet et al., 2021; Patton et al., 2016~~) (Ziemen et al., 2014; Quiquet et al., 2021; Gandy et al.). Therefore, to investigate climate-ice sheet interactions during the LGM, an earlier time period within this 6 ka interval may be

more representative. To this end, we present two simulations for the LGM, one for the onset of the LGM, 26 ka BP (LG-26ka) and one for the end, 21 ka BP (LG-21ka). Our aim is to provide a detailed simulation of the climate, surface energy fluxes and SMB components of the LGM ~~northern hemisphere~~ Northern Hemisphere ice sheets and evaluate the differences between the LG-21ka, the standard reference for the LGM period and the LG-26ka.

60 The paper is structured as follows. Section 2 describes the model and simulation design. Section 3 presents the simulation of global climate. Section 4 shows the analysis of the SMB of the ice sheets. Section 5 contains the discussion and conclusions.

2 Method

2.1 Community Earth System Model 2.1

All results in this paper are from ~~CESM2~~ CESMv2.1 (CESM2.1; Danabasoglu et al., 2020), a model which includes components
65 for the atmosphere, ocean, sea ice, land, and ice sheets. The model has participated in the Climate Model Intercomparison Project 6 (CMIP6). Of the CMIP6 models, it is the only model providing an interactive calculation of the Greenland ice sheet (GrIS) SMB for all simulations and dedicated interactive GrIS simulation (Sellewold and Vizcaíno, 2020).

The atmosphere is simulated by a hybrid version of the Community Atmosphere Model (~~CAM; Danabasoglu et al., 2020~~)
(CAM5; Danabasoglu et al., 2020) that combines version 5 (CAM5) physics, ~~combined~~ with the sub-grid orographic form drag
70 parameterization of CAM6. CAM5 physics was preferred over the standard CAM6 that was used in CMIP6 simulations due to the CAM6 physics yielding unrealistically high cooling under last glacial forcings (Zhu et al., 2021). This excessive cooling (~~due to high equilibrium climate sensitivity~~) is due to a high equilibrium climate sensitivity of 5.3 K that has been attributed to updates in cloud parameterizations introduced in CAM6 (Gettelman et al., 2019; Zhu et al., 2022). A detailed comparison of CAM5 and CAM6 simulation of contemporary polar climate is given in Lenaerts et al. (2019).

75 The land model used in our simulations is the Community Land Model version 5 (CLM5; Lawrence et al., 2019). We turn off the anthropogenic influence (e.g., harvesting and irrigation) on vegetation. We use the River Transport Model (RTM; Hurrell et al., 2013) rather than the default and more advanced Model for Scale Adaptive River Transport (MOSART), as the latter requires high-resolution input, which is not available for the LGM. CLM5 calculates the SMB over the ice sheets via an energy-balance ~~calculated for melt and~~ model and uses an advanced simulation of snow and firn processes (van Kampenhout et al., 2017). The model simulates ~~realistically simulates~~ realistic contemporary ice sheet climate and SMB (van Kampenhout et al., 2020) and has been applied to projections for the GrIS (Muntjewerf et al., 2020, Muntjewerf et al., 2020b, Sellewold et al., 2020). Sub-grid variations in the SMB are simulated with the use of ten elevation classes (Sellewold et al., 2019). These elevation classes are active in CLM5 grid cells where both the land ice model is active and there is land-ice present. We make two minor modifications to the default settings for the elevation classes parameterizations (van Kampenhout et al., 2020) with
85 the aim of reducing the magnitude and extent of the ablation zone. The first modification is an increase of the bare ice albedo from 0.4 to 0.5. The former relative low albedo used in Greenland simulations (van Kampenhout et al., 2020) was partially motivated to account for the low albedo in the "dark zone" of the present-day southwestern ablation area. Second, we use different thresholds for repartitioning the precipitation phase between snow and rain. Precipitation falls exclusively as rain

above 2°C and snow below 0°C, with mixed-phase precipitation between this range. These repartition thresholds are the same
90 as used over vegetation by default in CESM2.1.

The atmosphere and land model are ran at a horizontal resolution of 0.9° (latitude) × 1.25° (longitude); the ocean model (POP2) and sea ice model (CICE5) are ran on a 1° displaced Greenland grid. In ~~the ocean model POP2~~ we do not include ocean biogeochemistry (MARBL) but the estuary model from Sun et al. (2017) is adopted. The overflow parameterization in POP2 (Danabasoglu et al., 2010) was adjusted from the model modern values due to the narrowing of Denmark Strait as a
95 result of the larger-than-present GrIS. Also, part of Baffin Bay was closed due to excessive sea-ice formation in connection with a narrower bay from the larger-than-present GrIS. This part is treated as covered with land ice.

The Community Land Ice Model version 2.1 (~~CISM2.1; Lipscomb et al., 2019~~) (CISMv2.1; Lipscomb et al., 2019) is used as a diagnostic component; i.e., we do not run with interactive ice sheets. The ~~4-km CISM~~ 24 km CISMv2.1 grid (Fig. A1) provides high-resolution information for CLM5's elevation classes, as well as downscaled SMB (at 4 km resolution) by horizontal bilinear and vertical interpolation from the elevation classes. (Note at present precipitation is not downscaled). In our
100 simulations we produce elevation class information for SMB, surface 2 m air temperature across the CISM2.1 grid (Fig. A1) of the Northern Hemisphere ice sheets but also across the Antarctic and Patagonia ice sheets (however the latter are not analysed here).

2.2 Model set up and boundary conditions

105 We ran two 500 ~~years-long simulations for year simulations for a~~ 26 ka BP (LG-26ka) and a 21 ka BP (LG-21ka) climate using the boundary conditions and glacial forcings listed in Table 1. The LG-21ka simulation was initialised using two published 21 ka CESM simulations for the climate and ocean (Table 1). The climate and ocean state at year 100 of LG-21ka was used as the initial conditions for LG-26ka. An offline glacial isostatic adjustment model (GIA, see general description in Whitehouse (2018)) was ran to produce the initial 21 ka input boundary conditions which define the paleocoastlines, topography, land-ocean
110 mask and ice sheet extent. The input ice sheet reconstruction used for the GIA model combines the Antarctic and Patagonia ice sheets from ICE5G (Peltier, 2004); the ~~North American ice sheet complex (NAISC), Laurentide (LIS), Cordilleran (CIS) and Innuitian (IS))~~ NAISC from GLAC1D (Tarasov et al., 2012), the GrIS from HUY3 (Lecavalier et al., 2014), and the Eurasian ice sheet complex (~~British and Irish, Scandinavian and Barents-Kara Sea~~ BIIS; BKIS and SIS) from BRITICE-CHRONO (Clark et al., 2022) (Fig.A1). The GIA model output was regridded to a reference 10 min grid (bilinear interpolation) following the
115 protocol as defined in PMIP4 (Kageyama et al., 2017, figure 3). An offline vegetation model (BIOME4; Kaplan et al., 2003) was ran with climate forcing from the ~~LG-21ka-LG-21 ka~~ simulation to generate the vegetation distribution (see Appendix B). ~~The overflow parameterization in POP (Danabasoglu et al., 2010) was adjusted from the model modern values due to the narrowing of Denmark Strait as a result of the larger-than-present GrIS. Also, part of Baffin Bay was closed due to excessive sea-ice formation in connection with a narrower bay from the larger-than-present GrIS. This part is treated as covered with~~
120 ~~land ice.~~

Table 1. Summary of boundary conditions and forcings used for the two simulations. For the LG-21ka and LG-26ka values were taken from Ivanovic et al. (2016).

Parameter setting	LG-21ka	LG-26ka
Solar constant	pre-industrial	pre-industrial
Eccentricity	0.018995°	0.017742 ¹
Obliquity	22.949°	22.31° ¹
Perihelion-180	114.42°	32.09° ¹
CO ₂ (ppm)	190	184 ²
CH ₄	375	355 ³
N ₂ O (ppb)	200	199 ⁴
Others (CFC)	0	0
Ozone	pre-industrial	pre-industrial
Vegetation	21ka ⁵	21ka ⁵
Land surface topography	21ka	21ka
Ice sheets	21ka	21ka
Ocean restart	CESM1 21ka ⁶	LG-21ka
Climate restart	CESM2 21ka ⁷	LG-21ka
Simulation length	500 years	500 years

¹ Berger (1978). ² Bereiter et al. (2015). ³ Loulergue et al. (2008). ⁴ Schilt et al. (2010). ⁵ Offline BIOME4 simulation Kaplan et al. (2003). ⁶ DiNezio et al. (2018). ⁷ Zhu et al. (2021)

3 Climate simulation

To evaluate the climate state from our two simulations, we compare the global average of a range of climate outputs from LG-21ka and LG-26ka to published proxy and model results (Table 2). Additionally, we ~~compare-evaluate~~ the spatial pattern of the global ~~surface-near-surface~~ temperature (SAT) ~~from-with-two-different~~ (Fig. 1), ~~sea surface temperature (SST) and sea-ice extent~~ (Fig. 2) ~~from LG-21ka to a range of published datasets. For the SST and sea-ice we have regridded the GLOMAP dataset (Paul et al. (2021)) onto our CESM grid. However we note that there is uncertainty in the GLOMAP sea-ice data that has not been fully quantified and we are using it only as a guide to assess our simulations. For SAT we use two datasets: (i) an alternative 21ka CESM2CESMv2.1 simulation (Zhu et al., 2021, refer to as LGM-Zhu) and (ii) proxy-constrained, full-field reanalysis from Osman et al. (2021) (refer to as Osman) (Fig. 1c+d). There are a number of differences in the model setup~~ between the two ~~CESM2CESMv2.1~~ 21 ka simulations (LG-21ka and LGM-Zhu): (i) the input vegetation dataset, with LGM-Zhu adopting a PI datasets all over the globe; (ii) the ice sheet reconstruction, with LGM-Zhu using the ICE6G as defined within the PMIP4 protocols. In ~~this-the ICE6G~~ reconstruction, the GrIS is smaller and does not extend beyond the present day

coastline ~~As and as~~ such the adjustments made within POP in our model setup ~~, narrowing of Baffin Bay and adjustment of the overflow parameterization (see Section 2.1)~~ are not required.

Table 2. Annual-means (20 years) of various quantities from LG-26ka and LG-21ka, CCSM4 (Brady et al. (2013)), PMIP4 (Kageyama et al. (2021)), and different proxy data. Standard deviations are given in the curly brackets; differences to their respective PI simulations in brackets. Note a latitudinal range of 30°S to 30°N was used for the tropical calculations

	LG-26ka	LG-21ka	CCSM4	PMIP4	Proxy
Global precipitation (mm day ⁻¹)	2.50 {0.01} (-0.58)	2.59 {0.01} (-0.49)	2.61 (-0.32)	2.72 ¹	
Tropical precipitation (mm day ⁻¹)	3.26 {0.01} (-0.48)	3.32 {0.02} (-0.42)	3.93 (-0.36)		
Global near-surface T (°C)	6.47 {0.09} (-8.30)	7.93 {0.11} (-6.84)	9.83 ¹		6.40 (-7.10) ⁵
Global surface T (°C)	7.39 {0.09} (-8.26)	8.86 {0.11} (-6.79)	9.04 (-4.97)	11.54 ²	
Tropical land surface T (°C)	21.42 {0.16} (-4.42)	22.28 {0.18} (-3.56)	20.89 (-2.61)		(-3.9) ⁸
GRIP (°C)	-42.38 {1.51} (-14.39)	-38.35 {1.48} (-11.36)	-37.76 (-8.54)		(-11.5) ⁷
Vostok (°C)	-62.35 {0.58} (-12.39)	-60.31 {0.72} (-10.35)	-62.84 (-9.97)		(-12) ⁶
Global precipitable water (mm)	17.14 {0.10} (-8.69)	18.30 {0.18} (-7.53)	18.84 (-5.09)		
Tropical SST (°C)		23.14 {0.14} (-3.35)	24.78 (-2.16)	23.30 ³	(-3.5) ⁸
AMOC at 30°N (Sv)	17.1	18.4	22	16-24	
Sea-ice area NH (×10 ⁶ km ²)	12.54 {0.39} (2.74)	9.39 {0.21} (-0.41)	8.64 (-3.06)		9.40 ⁴
Sea-ice area SH (×10 ⁶ km ²)	29.65 {0.47} (20.65)	25.87 {0.41} (16.87)	27.88 (10.9)		24.72 ⁴

¹ AWI-ESM-1-1-LR, INM-CM4-8, MIROC-ES2L, MPI-ESM1-2-LR. ² MIROC-ES2L

³ MIROC-ES2L, MPI-ESM1-2-LR. ⁴ Paul et al. (2021). ⁵ Osman et al. (2021). ⁶ Petit et al. (1999). ⁷ Lecavalier et al. (2014). ⁸ Tierney et al. (2020)

135 An average global near-surface cooling of ~~6.84~~6.8°C is simulated by the ~~last two decades of the~~ LG-21ka simulation (Fig. C1, Table 2), which agrees well with the results from the two comparison datasets; Osman ~~77.1±1°C~~ and 6.5°C LGM-Zhu, ~~and and~~ ~~this recent study~~ Liu et al. (2023). ~~This simulation~~ is significantly colder ~~everywhere than in (lower temperature) everywhere than the~~ PI (Fig. 1a). ~~The shows polar amplification of cooling in both seasons, but strongest in the winter), with the cooling amplified across the polar regions in both season (Fig. C2). Most of the cooling, in both seasons, occurs over the ice sheets that are not present in the PI simulation. The largest reduction in temperature (cooling) is across the glaciated regions (North America, Eurasia and Antarctica) due to the higher elevations and the change from vegetated surfaces to ice surfaces (relative to PI). This is in contrast with contemporary polar amplification of global warming, where the highest increases in winter near-surface temperatures take place over the Arctic Ocean. In the Northern Hemisphere summer, the 0°C isotherm correspond well to the southern margin of the ice sheets (Fig. C2c).~~

145 When comparing the LG-21ka results to LGM-Zhu and Osman, we find some notable spatial differences (Fig. 1c,d). ~~The lower surface elevation across the ice sheet regions and narrowing of Baffin Bay in the SAT which approximately corresponds to the differences in elevation between the two simulations (Fig. 1) results in a cooling in compared to (Fig. 1c), up to 7°C across BKIS and 16°C in Baffin Bay. C3). The lower (colder) temperatures around the margin of the ice sheet are associated~~

with higher elevations (and vice versa). However we note it is not an exact 1-1 relationship. The differences across the surface of the large ocean basins are small, less than $\pm 0.5^\circ\text{C}$, but as Section 3.3.3.2 describes, there are differences in the deep ocean circulation. Relative to the Osman study, LG-21ka is colder (lower temperatures) across AIS and the southern ocean (up to 7°C), but is warmer (higher temperature) across central Pacific Ocean, North Atlantic (up to 11°C) and the Arctic Ocean (8°C). The largest warm anomalies are across the Northern hemisphere ice sheet region, up to 20°C across the centre of the CIS Cordillerin ice sheet (CIS) and 12°C across LIS, the former of which coincides with Laurentide ice sheet (LIS). Note that these regions coincide with the highest standard deviations from the model ensemble, (up to 9°C) in the SAT from the ensemble of models performed by Osman et al., (2021). There is an anomalous cold zone extending from the southern coast of Greenland relative to both comparison datasets, the extent of which coincides with relatively large summer Arctic sea ice extent (Section 3.23.1).

The LG-26ka simulation is 1.5°C colder than LG-21ka (global average), enhanced at higher latitudes, with a 4°C and 2°C cooling at the location of the GRIP and VOSTOK ice core sites, respectively. The largest anomalies are concentrated across the North Atlantic (decrease of 6°C) along the eastern margin of the GrIS and Siberia (decrease of up to 8°C) (Fig. 1b). In terms of the ice sheets, there is a cooling along the southern margin of the NAISC of 1°C , compared to 3°C across the BIIS, EuIS, and BKIS, which, as we evaluate in Section 4.1 has important implications for the simulated SMB.

~~Annual means of various quantities for the last 20 years of the simulations and refers to our CESM2.1 simulation, CCSM4 to a simulation by Brady et al. (2013), PMIP4 to simulations by Kageyama et al. (2021), and Proxy to the different proxy data. Standard deviations are given in the curly brackets; differences to their respective PI simulations in brackets. LG-26ka CCSM4 PMIP4 Proxy Global precipitation (mm day^{-1}) 2.50 {0.01} (-0.58) 2.59 {0.01} (-0.49) 2.61 (-0.32) 2.72¹ Tropical precipitation (mm day^{-1}) 3.26 {0.01} (-0.48) 3.32 {0.02} (-0.42) 3.93 (-0.36) Global near-surface T ($^\circ\text{C}$) 6.47 {0.09} (-8.30) 7.93 {0.11} (-6.84) 9.83¹ 6.40 (-7.10)⁵ Global surface T ($^\circ\text{C}$) 7.39 {0.09} (-8.26) 8.86 {0.11} (-6.79) 9.04 (-4.97) 11.54² Tropical land surface T ($^\circ\text{C}$) 21.42 {0.16} (-4.42) 22.28 {0.18} (-3.56) 20.89 (-2.61) (-3.9)⁸ GRIP ($^\circ\text{C}$) -42.38 {1.51} (-14.39) -38.35 {1.48} (-11.36) -37.76 (-8.54) (-11.5)⁷ Vostok ($^\circ\text{C}$) -62.35 {0.58} (-12.39) -60.31 {0.72} (-10.35) -62.84 (-9.97) (-12)⁶ Global precipitable water (mm) 17.14 {0.10} (-8.69) 18.30 {0.18} (-7.53) 18.84 (-5.09) Tropical SST ($^\circ\text{C}$) 23.14 {0.14} (-3.35) 24.78 (-2.16) 23.30³ (-3.5)⁸ AMOC at 30°N (Sv) 17.1 18.4 22 16-24 Sea-ice area NH ($\times 10^6 \text{ km}^2$) 12.54 {0.39} (2.74) 9.39 {0.21} (-0.41) 8.64 (-3.06) 9.40⁴ Sea-ice area SH ($\times 10^6 \text{ km}^2$) 29.65 {0.47} (20.65) 25.87 {0.41} (16.87) 27.88 (10.9) 24.72⁴~~

175 3.1 Sea surface conditions

Both our simulations overestimate the mean monthly sea-ice extent relative to GLOMAP, (Fig. 2b+d, Table. 2), with the area increasing in the colder (lower) temperatures of LG-26ka and during the summer season. The timings of the Northern (Fig. 2b) and Southern Hemisphere (Fig. 2d) maximum and minimum sea ice extent are the same as for present day but are delayed by one month relative to GLOMAP. Spatially, the differences are more complicated. During the summer in both the Northern and Southern Hemisphere, LG-21ka overestimates the spatial extent of the sea ice (Fig. 2a and c). For example, there are large areas of sea-ice across the Norwegian and Greenland seas, which are ice free in GLOMAP. In the winter months, the simulation underestimates in these regions, but overestimates across the Bering Sea, Baffin Bay and into the Labrador Sea.

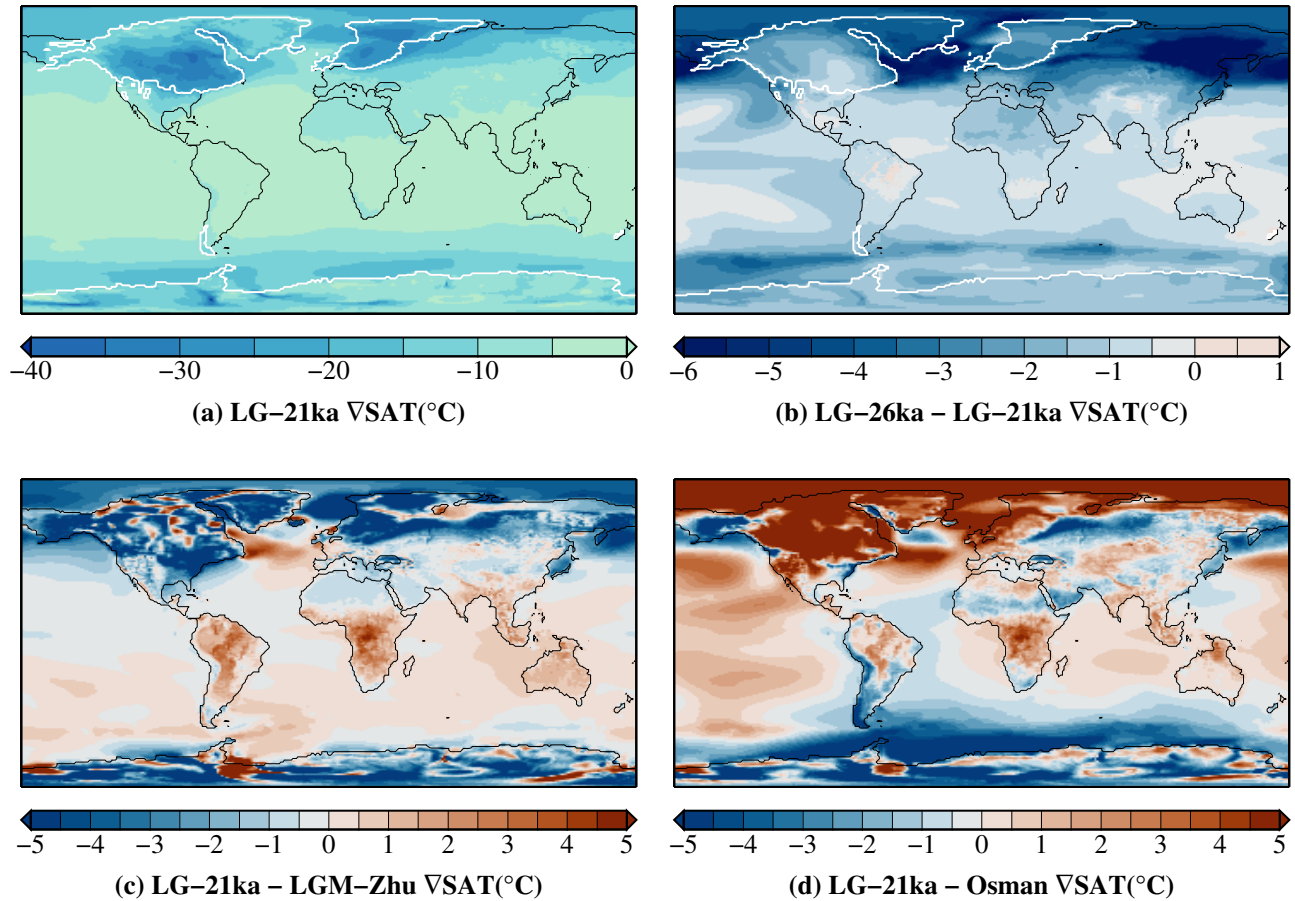


Figure 1. Annual-mean (20 years) near-surface air temperature (SAT $^{\circ}$ C) anomalies with respect to pre-industrial for (a) the LG-21ka simulation (30-yr average). The black contour is the paleocoastline, the white contour encloses the glaciated regions and the dashed-black contour lines are every 10° C. (b) Differences between LG-26ka and LG-21ka. Solid white contours are every 2° C. (c) Difference Differences between LG-21ka and LGM-Zhu, dotted black contour is the 0° C; White contour marks 5° C LGM-Zhu. (d) Difference between LG-21ka and SAT taken from Osman et al. (2021) (regridded to the CESM grid)

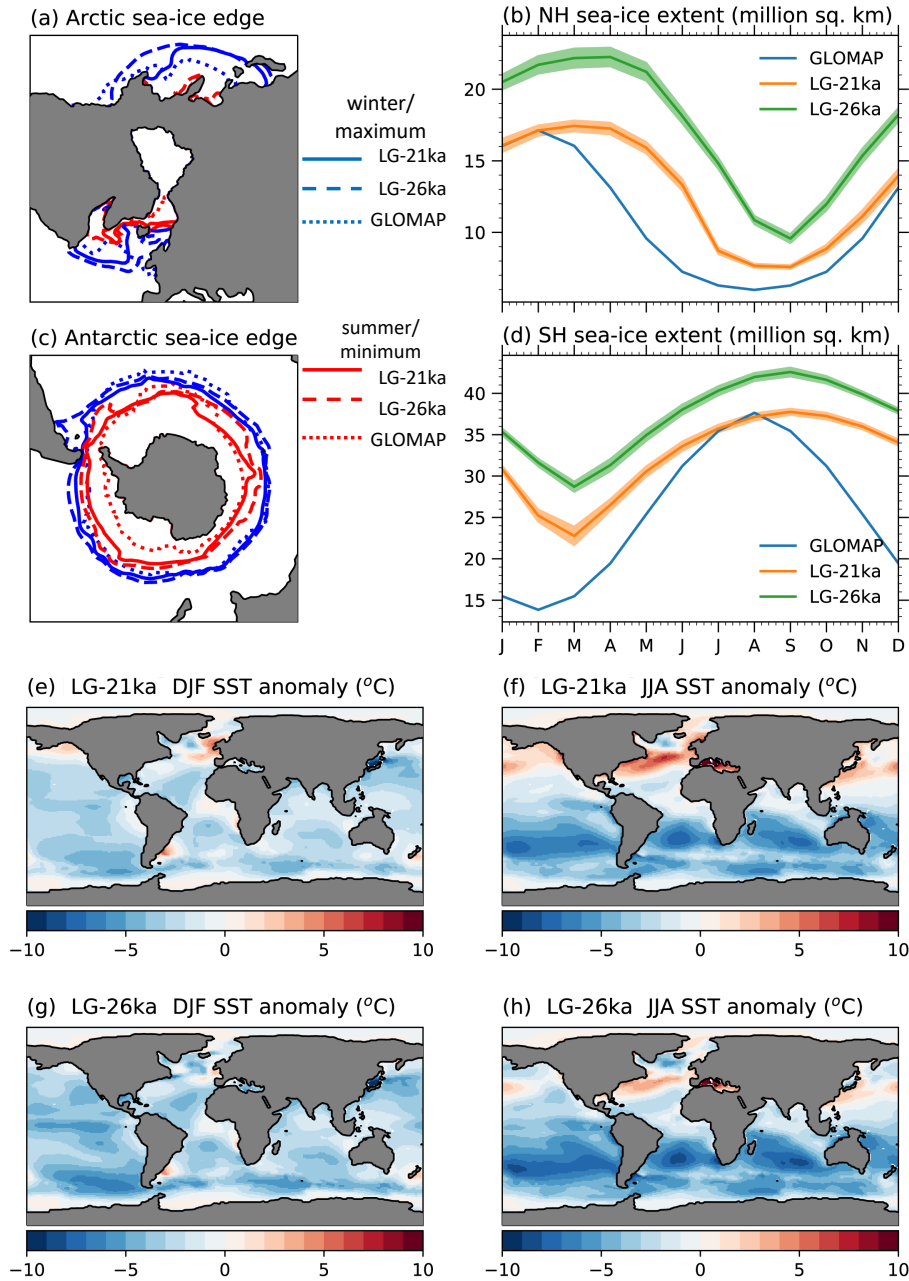


Figure 2. Comparison of sea-ice and SSTs between LG-21ka and LG-26ka and GLOMAP (Paul et al., 2021). (a,c) Shows sea-ice edge ($>15\%$ sea-ice concentration) for the maximum/winter extent (blue) and minimum/summer extent (red), with LG-21ka in solid lines, LG-26ka in dashed lines and GLOMAP in dotted lines. (b,d) Shows the mean (20 years) sea-ice extent for the Northern and Southern Hemispheres per month of the year. (e-h) Shows the DJF and JJA SST anomalies ($^{\circ}\text{C}$), where the anomalies are the difference between LG-21ka and LG-26ka and GLOMAP, and their respective pre-industrial values.

185 Generally, LG-21ka simulates alower (colder) ocean temperatures than GLOMAP (Fig. 2e-f) across large areas of the ocean, with the global mean SST -2.2°C and -2.4°C colder in winter and summer respectively. This colder ocean may be one cause for the consistent overestimation in the sea-ice extent. There are warm anomalies (reaching up to 8°C), which are predominately concentrated in the Northern hemisphere, extending from the NAISC across the North Atlantic to the BIIS and extending from the North Pacific ocean (the Gulf of Alaska and Bering Strait) across to the sea of Japan.

3.2 Atlantic Meridional Overturning Circulation

190 The AMOC strength (defined as the maximum AMOC transport at 30°N) is weaker and the extent of the overturning cell shallower in all three LGM simulations relative to the PI (Figure 3b). The maximum strengths are 18.4 Sv, 17.1 Sv and 16.6 Sv for LG-21ka, LG-26ka and LGM-Zhu, (Figure 3b) respectively. As stated earlier, the LG-21ka and LGM-Zhu simulations adopted different ice sheet reconstructions with the former including a revised overflow parameterization around Baffin Bay and the Denmark Strait. A recent publication (Kapsch et al., 2022) found that the ICE6G reconstruction (similar to LGM-Zhu) resulted in a stronger AMOC relative to GLAC1D (similar to LG-21ka) due partly to higher elevation across the NAISC complex. This is opposite of the results from this comparison, which highlights the complex non-linear interplay between the change in elevation across glaciated regions and the resultant impact on sea-ice extent and AMOC strength (Sherriff-Tadano et al., 2018; Sherriff-Tadano and Abe-Ouchi, 2020; Zhu et al., 2014). Two recent transient simulations for the LGM period found either no change in the AMOC between 26 ka and 21 ka BP (Kapsch et al., 2022) or a minor weakening (Quiquet et al., 2021) which is similar to our findings.

200 The maximum extent of the overturning cell, defined as the depth for which the AMOC strength (at $\sim 30^{\circ}\text{N}$) is positive, shoals by ~ 240 m for LG-21ka and LG-26ka and by 480m in LGM-Zhu. (Figure 3b). The shoaling of the simulated glacial AMOC compared to the PI simulation is in agreement with most of the earlier LGM studies (e.g. Muglia and Schmittner, 2021; Gu et al., 2021).

205 Evaluating the AMOC strength from a depth-latitude view point (Figure 3c-e), south of $\sim 50^{\circ}\text{N}$ the AMOC is weaker and shallower in all three LGM simulations (LG-21ka, LG-26ka and LGM-Zhu), while north of $\sim 60^{\circ}\text{N}$ its signal is stronger and of similar vertical extent. Therefore, some of the differences between different studies resultant may result from not adopting the same definition for the AMOC. Previous studies have suggested that the process of deep convection in the Labrador Sea is affected by the advancing of the sea-ice in the lower temperatures of the glacial climate which in turn impacts the AMOC strength and geometry (Klockmann et al., 2018). As stated above, this is a region where LG-21ka overpredicts the extent of the sea-ice (Fig. 2a). Indeed, the winter mixed layer depth averaged over the subpolar North Atlantic is shallower by ~ 400 m in the glacial simulations compared to PI (Figure C5a-c). Therefore our weaker AMOC may result from the overestimation of sea-ice which limits the deep water formation producing a weaker overturning cell compared to PI. In the Nordic Seas, north of $\sim 60^{\circ}\text{N}$, the winter mixed layer depth is deeper in the glacial simulations compared to PI (Figure C5a-c) which corresponds to the region of stronger AMOC $\sim 60^{\circ}\text{N}$ (Figure 3c-e). ~~Dotted black contour is~~

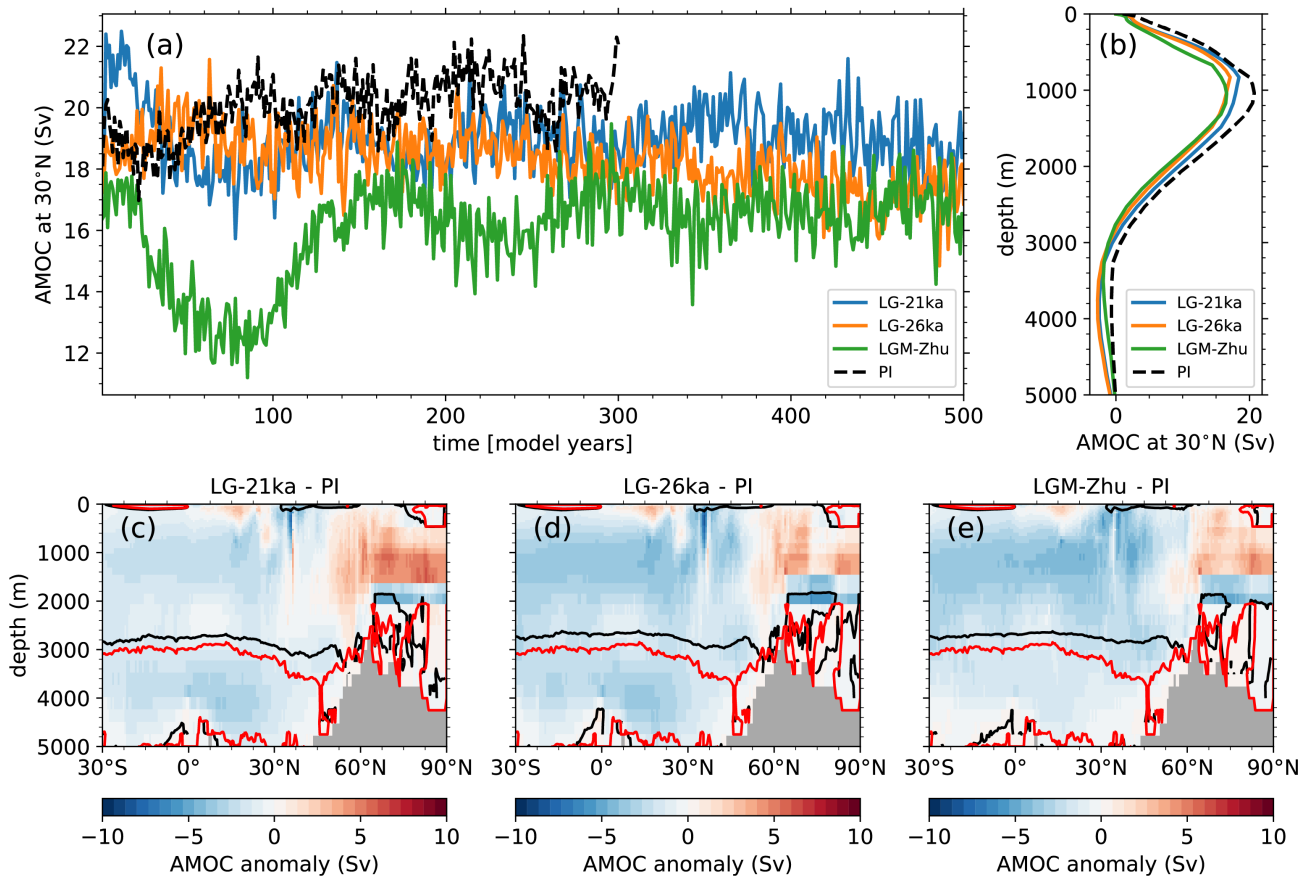


Figure 3. AMOC strength (defined as the θ maximum AMOC transport at 30°EN) as a function of (a) time and (b) depth for LG-21ka (blue line), LG-26ka (orange line), LGM-Zhu (green line) and PI (black line). (c-e) AMOC anomaly as a function of latitude and depth (in Sv; The white contours-0 Sv contour line in black for LG-21ka and in red for PI) for (c) LG-21ka, (d) LG-26ka and (e) LGM-Zhu with respect to the PI simulation. Values in (b-e) are averaged over the standard deviation from the model ensemble, 1°C interval and 20 years of each simulation.

215 3.3 Atmospheric simulation: radiation, clouds and circulation

The top-of-the-atmosphere insolation ($\text{TOA } SW_{in}$) that forces the 21-ky climate is substantially different from pre-industrial, due to the different orbital conditions. The LG-21ka simulation $\text{TOA } SW_{in}$ is reduced (less insolation) with respect to PI at northern and southern high latitudes during May-October and October to March, respectively (Fig. 4a). Tropical and subtropical regions experience a small positive change in insolation for most months, except between August-October where they have a small negative change in insolation. During these periods of reduced $\text{TOA } SW_{in}$ at northern and southern latitudes (-10 W m^2), there is an a much larger increase in the surface SW_{in} (Fig. 4a). Changes in atmospheric and surface

220

conditions explain these and other large differences between TOA and surface SW_{in} . By comparing differences in the SW_{in} flux under all-sky and clear-sky conditions b), up to 100 m^2 , which can be linked primarily to changes in the cloud cover (Fig. 4a,b), we find that the changes in cloud cover are the main contributor to the larger surface SW_{in} . In addition c). Additionally, 225 the presence of the extensive LGM ice sheets (Fig. A1) ~~;~~ as well as combined with the increase in the spatial extent of sea-ice ~~extending further into the midlatitudes into the mid latitudes~~ (see section 3.1) ~~increase~~ increases the surface albedo (see Fig. 8f) ~~-. This increase allows for~~ which allows more multiple scattering and ~~thereby increases surface~~ SW_{in} . Furthermore, the colder LGM atmosphere holds less water vapor (Table 2), also contributing to increases in the ~~therefore also contributes to the~~ increase the surface SW_{in} . In all high latitude regions showing enhanced surface SW_{in} , SW_{net} ~~is however~~ (Fig. 4d) is reduced 230 due to overcompensation from higher surface albedo (Fig. 4e8f).

The surface incoming longwave radiation (LW_{in} , Fig. 4de) is reduced at all latitudes and times of the year with respect to PI with the largest anomalies corresponding to the areas of largest cooling over the ice sheets (Fig. 1a) and expanded sea-ice cover. The temporal and latitudinal pattern of surface net longwave radiation (LW_{net} , Fig. 4ef) shows both positive and negative anomalies (positive corresponds to net radiation gain by the surface), with net radiation loss over the northern hemisphere ice 235 sheets during the summer, and in the Tropics all over the year. The magnitude of this summer reduction in LW_{net} over the ice sheets is smaller than for SW_{net} .

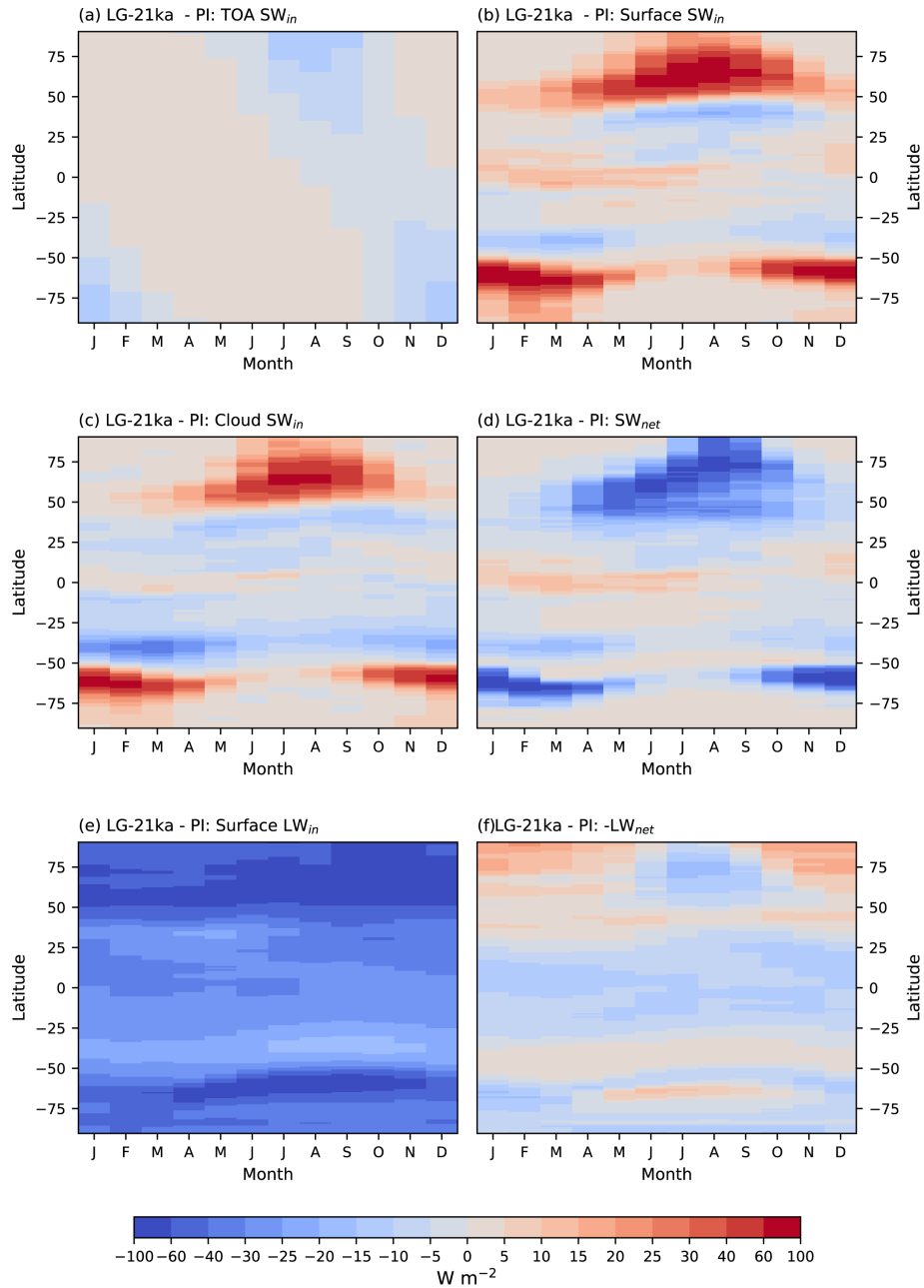


Figure 4. Monthly zonal means (20 years) of (a) Top of the atmosphere (TOA) incoming solar radiation (SW_{in}), (b) incoming solar radiation at the surface (SW_{in}), (c) cloud contribution to incoming solar radiation at the surface (SW_{in}), (d) net shortwave radiation at the surface (SW_{net}), (e) incoming longwave radiation at the surface (LW_{in}), (f) net longwave radiation at the surface (LW_{net}). For all panels, positive values (red) indicate energy gain by the surface. Total radiation change at the surface results from the addition of panels c and e.

We continue our analysis of atmospheric change by examining changes in the atmospheric circulation (asymmetrical component of the geopotential height) and their connections with cloud change. ~~To this end, we compare changes in the asymmetrical component of the geopotential heights between and PI~~ (Fig. 5). Around the NAISC, two circulation anomalies appear (Fig. 240 5a+b). On the western side-coast of North America across the CIS, the PI winter ridge is intensified and extends further towards Asia. The winds associated with this ridge transports warm and moist air from the Pacific to Alaska. ~~On the eastern side, across~~ Across the east coast of North America and the LIS, a negative response occurs, due to the strengthening and southward elongation of the Greenland climatological low, extending the persistent inflow of Arctic air towards the North Atlantic margin. This response strengthens the geopotential gradient between the Atlantic and LIS, suggesting higher wind speeds of the polar 245 jet.

The winter climatological ridge (Fig. 5a) which brings warmer (higher temperature) and moister air from the North Atlantic towards Europe is weakened along its northern flank, which results in drier and colder Arctic air over Northern Europe. On the Asian side, the Aleutian low is weakened. The summer circulation responses (Fig. 5b) are weaker than in winter. There is a negative response over LIS, which represents a narrowing of the Rocky mountain ridge and a strengthening and enlarged 250 Greenland low. This change in summer circulation ~~produces the colder condition over~~ results in a reduction in temperature across LIS during the LGM (Fig. 1a). There is a positive response in the North Atlantic which extends across the BIIS. As both these responses strengthen the PI climatological features, they sharpen the geopotential gradients and give rise to higher wind speeds, which is indicative of increased synoptic eddy activity.

~~We find similar~~ The circulation anomalies in ~~the LG-26ka simulations and as such, suggest that these features may be caused by a combination of several factors, such as differences in land-sea configuration, topography, as well as thermal contrasts. are~~ very similar which suggests they are not strongly influenced by the changes in orbital forcing. 255

~~As we saw, clouds play an important role in regulating surface radiation fluxes. Cloud effects largely depend on their liquid water (efficient at blocking~~ To investigate further the influence of clouds on the radiation fluxes, we examined the change in cloud liquid and ice content (Fig. 5d and e). Clouds with a higher liquid content will block incoming solar radiation) and ice 260 ~~(, where as ice is nearly transparent to incoming solar radiation) content.~~ During the summer, there is very little cloud liquid water across the ice sheets (Fig. 5c), a significant reduction compared to the PI (Fig. 5d). This is caused by the increase in elevation, a relatively high cloud liquid water in the PI, as well as the negative circulation anomalies (Fig. 5b) making these areas receive more dry and cold Arctic air. Therefore the positive anomalies in the SW in (Fig. 4a) are in part due to a reduction in cloud liquid. Conversely there is an small increase in cloud ice water (Fig. 5e+f), a feature that is common over current ice 265 sheets, due to the colder (lower) temperatures and higher elevation (Ettema et al., 2010; Lenaerts et al., 2019).

~~Annual means (20 years) for atmospheric water content. a) and b) shows precipitable water (kg m^{-2}), while c) and d) shows large-scale precipitation (mm yr^{-1}). The left column shows values from the simulation, while the right column shows the differences between and the PI simulations. Grey contour encloses glaciated areas (>50% ice cover). Patched areas show where differences are non-significant at the 99% level according to a student's t-test.~~

270 ~~The amount of annual mean precipitable water (i.e., the vertically integrated atmospheric humidity) decreases everywhere with respect to PI, and globally at 21 ka BP by 7.53mm (0.18 s.d) (Table2 and Fig. ??b). This is a consequence of the global~~

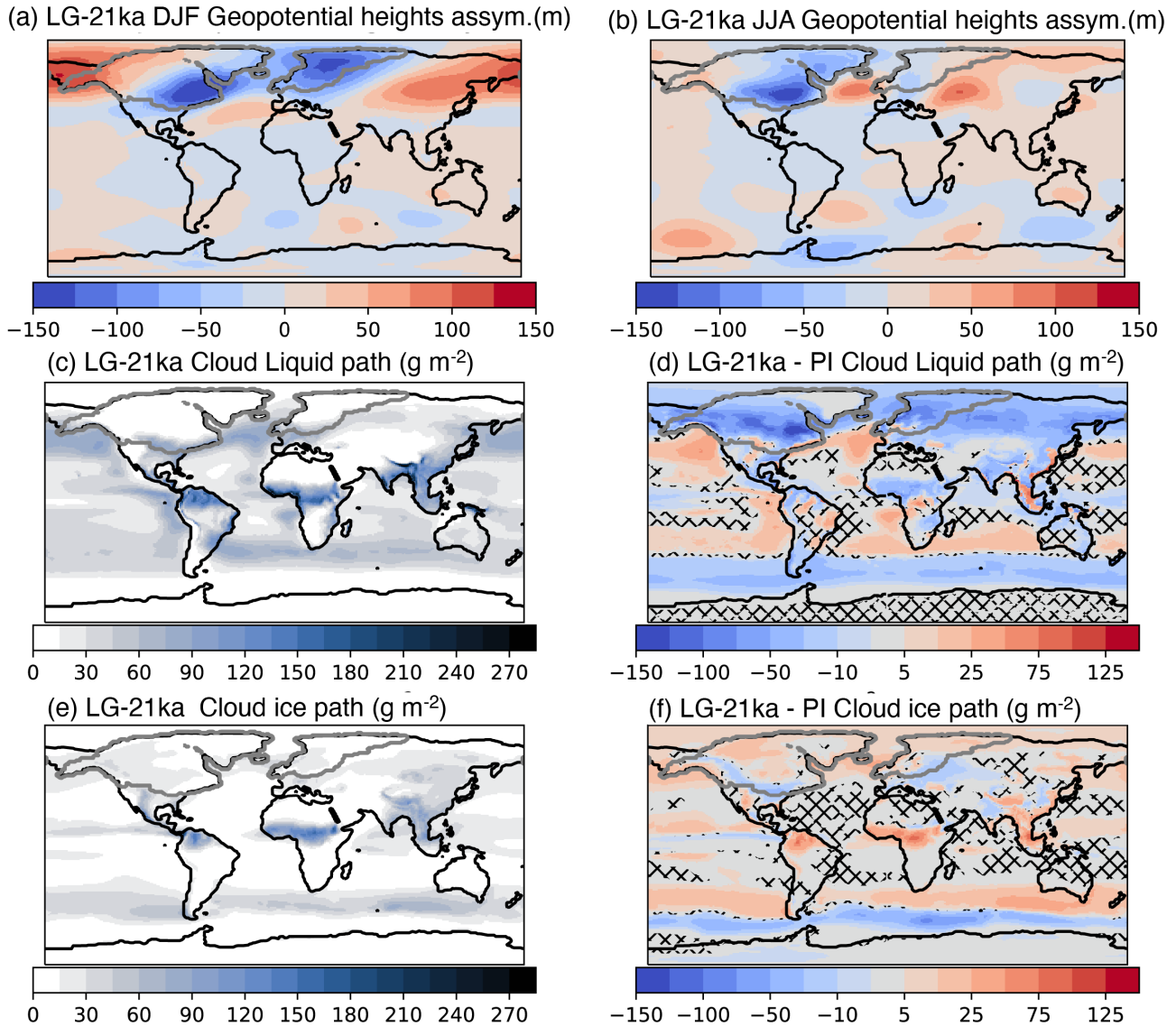


Figure 5. Geopotential height anomalies (relative to PI) (m) after subtracting the zonal means (20 years) (a) DJF and (b) JJA. [Note we analyze the geopotential height at an atmospheric pressure of 200 hPa.](#) Panels (c - f) are relative to the Summer mean clouds. (c) and (d) shows cloud liquid path, while (e) and (f) shows cloud ice path, all in g m^{-2} . The left column shows values from the LG-21ka simulation, while the right column shows the differences between LG-21ka and the PI simulations. Grey contour encloses glaciated areas (>50% ice cover). Patched areas show where differences are non-significant at the 99% level according to a student's t-test relative to the month variations.

cooling, as a colder atmosphere can hold less water. The largest decreases occur in the tropics and over the southern parts of the ice sheets. The large reduction in the tropics is due to the relatively high amounts of precipitable water there in the PI. Over the ice sheets, the large reduction in precipitable water relates to large elevation change and cooling.

275 Although precipitable water decreases everywhere, some areas experience higher annual mean large-scale precipitation rates. We focus on large-scale precipitation (Fig. ??e), as this is the main process for generating precipitation over the ice sheets, with convective precipitation playing a much smaller role. Increases in precipitation occurs along the southern margins of the NAISC, BHS and SIS (Fig. ??d). These increases are likely associated with changes in circulation. As seen earlier, there is more advection of Pacific air, which increases precipitation. On the eastern margin of the LIS, we see increase of wind speeds,
280 which can indicate more synoptic activity. Further, the steep and higher elevation together with the associated cooling inwards on the ice sheet, can force precipitation to fall at the margins. Over the SIS, synoptic systems move, on average, more along the margin of the ice sheet, while in PI they could move further north. This possibly explains the response of increased precipitation along the margins and the drier conditions in the North.

In summary, we see large differences in circulation, clouds, temperature, and precipitation between the LG-21ka and PI
285 climates, some of them largely connected with the presence of large ice sheets in the northern hemisphere. The circulation in LG-21ka suggests more advection of Pacific air towards Alaska, bringing more moisture which increases precipitation and thickens clouds. ~~The~~ In the interior of the Laurentide-NAISC (across the Laurentide ice sheet) experiences an anomalous trough, which likely brings in drier Arctic air, leading to thinning of clouds, less precipitation, and much ~~colder~~ lower(colder) air temperatures than in PI. In LG-21ka ~~colder conditions are simulated~~ the temperatures are lower around Greenland, particularly
290 in the West where the PI low gets strengthened. The Eurasian ice sheets experience similar responses as the Laurentide: wetter in the south, drier in the interior and north.

3.4 Sea surface conditions

Comparison of sea-ice and SSTs between and and GLOMAP (Paul et al., 2021). (a,c) Shows sea-ice edge (>15% sea-ice concentration) for the maximum/winter extent (blue) and minimum/summer extent (red), with in solid lines, dashed line and
295 GLOMAP dotted lines. (b,d) Shows the mean (20 years) sea-ice extent for the Northern and Southern Hemispheres per month of the year. (e-h) Shows the DJF and JJA SST anomalies ($^{\circ}\text{C}$), where the anomalies are the difference between and and GLOMAP, and their respective pre-industrial values.

To evaluate the ocean from our simulations, we compare our against sea surface temperatures (SSTs) and sea-ice extent from a global climatology of the ocean surface during the LGM mapped on a regular grid (Paul et al., 2021) (refer to as GLOMAP,
300 where the LGM is defined as the interval between 23ka and 19ka BP). Both the Northern and Southern Hemisphere global average sea-ice area from are overestimated relative to GLOMAP, with the area increasing in the colder simulation (Fig. 2b+d, Table. 2). When comparing the Northern Hemisphere monthly variability (Fig. 2b), the timings of our maximum (March) and minimum (September) extent matches the case for the present-day but are one month later than recorded by GLOMAP, February and August respectively. There is a similar difference in the timings of the maximum/minimum in the Southern
305 hemisphere monthly extents (Fig.2d).

For the Arctic region, there are some obvious differences between and GLOMAP. The summer sea-ice extent (compare red solid and dashed lines (Fig. 2a)) is overestimated in our simulations, covering large parts of the Norwegian and Greenland Seas, which are ice free in GLOMAP. In winter (compare blue solid and dashed lines (Fig. 2a)), overestimates sea-ice in the region south of Greenland, extending from Baffin Bay into the Labrador Sea, but underestimates across the Norwegian and Greenland seas. Across the Pacific ocean, the summer sea-ice extent is small and agrees well with the GLOMAP ice-free conditions. In winter, however, we overestimate within the Northwest Pacific, across the Bering Sea, but underestimate within the Gulf of Alaska, simulating sea-ice-free conditions.

In the Southern Hemisphere, differences with GLOMAP are smaller, with the sea-ice extent within the Indian Ocean a closer match to the results from GLOMAP. Regardless of the season, our model overestimates the sea-ice in the Pacific sector, but underestimates in the Atlantic ocean in relationship with GLOMAP.

Generally, simulates colder ocean conditions than GLOMAP (Fig. 2e-f) across large areas of the ocean, with the global mean SST -2.2°C and -2.4°C colder in winter and summer respectively. This colder ocean may be one cause for the consistent overestimation in the sea-ice extent. There are warm anomalies (reaching up to 8°C), which are predominately concentrated in the Northern hemisphere, extending from the NAISC across the North Atlantic to the BHS and extending from the North Pacific ocean (the Gulf of Alaska and Bering Strait) across to the sea of Japan.

3.4 Atlantic Meridional Overturning Circulation

In a recent study within the framework of the Paleoclimate Modelling Intercomparison Project (PMIP4, Kageyama et al., 2021) it was found that most of the models of the PMIP4 ensemble simulate a weaker and shallower overturning cell than in the PMIP3 simulations but all are stronger than the PI. In this subsection, we evaluate the simulated glacial AMOC state and we discuss the AMOC response to changes in orbital forcing (i.e. and) and the prescribed glacial continental ice sheets (i.e.).

The simulated AMOC strength (defined as the maximum AMOC transport at 30°N) is in a rather stable state during the last ~ 200 years of all simulations (Figure 3a). In the following, we analyze averages of the last 20 years of each simulation.

The AMOC strength is weaker and the extent of the overturning cell shallower in all three LGM simulations relative to the PI (Figure 3b). The maximum strengths are 18.4 Sv, 17.1 Sv and 16.6 Sv for , and , (Figure 3b) respectively. As stated earlier, the and simulations adopted different ice sheet reconstructions from PMIP4: GLAC1d (modified, see section 2.2) and ICE6G respectively and the former has a revised circulation around Baffin Bay and Denmark Strait due to the larger-than-present GrIS. A recent publication (Kapsch et al., 2022) found that the ICE6G reconstruction resulted in a stronger AMOC, relative to GLAC1D due partly to higher elevation across the NAISC complex. This is opposite of the results from this comparison, which highlights the complex non-linear interplay between the change in elevation across NAISC and EuIS and the resultant impact on wind speed, sea-ice extent and AMOC strength (Sherriff-Tadano et al., 2018; Sherriff-Tadano and Abe-Ouchi, 2020; Zhu et al., 2014)

The maximum extent of the overturning cell, defined as the depth for which the AMOC strength (at $\sim 30^{\circ}\text{N}$) is positive, shoals by ~ 240 m for and and by 480m in . (Figure 3b). The shoaling of the simulated glacial AMOC compared to the simulation is in agreement with most of the earlier LGM studies (e.g. Muglia and Schmittner, 2021; Gu et al., 2020).

340 The AMOC in a depth-latitude view highlights the above mentioned difference (all results are relative to PI) (Figure 3c-e).
These results also stress the importance when comparing publications to ensure the same definition for latitude and depth is
adopted for the AMOC. South of $\sim 50^\circ\text{N}$ the AMOC is weaker and shallower in all three LGM simulations (–, and –), while
north of $\sim 60^\circ\text{N}$ its signal is stronger and of similar vertical extent. Previous studies have suggested that the process of deep
convection in the Labrador Sea is affected by the advancing of the sea-ice in the colder glacial climate and in turn impacts
345 the AMOC strength and geometry (Klockmann et al., 2018). As stated above, this is a region where overpredicts the extent of
the sea-ice (Fig.2a). Indeed, the winter mixed-layer depth averaged over the subpolar North Atlantic is shallower by ~ 400 m
in the glacial simulations compared to (Figure C5a-e). That means that in the glacial simulations the formation of deep water
masses is limited in this region resulting in a weaker overturning cell compared to –. However, in the Nordic Seas the winter
mixed-layer depth is deeper in the glacial simulations compared to (Figure (C5a-e) explaining the stronger AMOC signal that
350 is evident north of $\sim 60^\circ\text{N}$ (Figure 3c-e).

In summary, we found that by changing the orbital forcing (i.e. and –) the AMOC strength weakens possibly due to a reduction
of the winter mixed-layer depth in the North Atlantic led by an increase of the sea-ice (Figure 3a-b, and Figure C5d, Figure
C6d). However, the vertical extent of the overturning cell is similar between and –. Two recent transient simulations for the
LGM period found either no change in the AMOC between 26 ka and 21 ka BP (Kapsch et al., 2022) or a minor weakening
355 (Quiquet et al., 2021).

AMOC strength (defined as the maximum AMOC transport at 30°N) as a function of (a) time and (b) depth for (blue line),
(orange line), (green line) and (black line). (c-e) AMOC anomaly as a function of latitude and depth (in Sv; 0 Sv contour line
in black for – and in red for –) for (c) –, (d) and (e) with respect to the simulation. Values in (b-e) are averaged over the last 20
years of each simulation.

360 Annual means from the last 20 years of simulation of a) surface mass balance, b) snowfall, c) rainfall, d) refreezing, e) melt,
and f) sublimation, all in mm yr^{-1} . Blue bars represent averages while orange bars represent averages, over the individual
ice sheets. North American ice sheet complex (Laurentide, Cordilleran and Innuitian (NAISC)), Greenland ice sheet (GrIS),
Barents-Kara Sea ice sheet (BKIS), Scandinavian ice sheet (SIS), British-Irish and northsea ice sheet (BIIS), and Icelandic ice
sheet (IcIS). The green and red dashed line correspond to present day GrIS and AIS averages (Mottram et al., 2021; Noël et al., 2020)
365 –. Note the annual means are scaled by ice sheet area (in units of mm yr^{-1}).

Maps of annual means from the last 20 years of simulation of (a) surface mass balance, (b) snowfall, (c) rainfall, (d)
refreezing, (e) melt, and (f) sublimation, all in mm yr^{-1} .

4 Northern hemisphere ice sheet surface mass and energy balance

In the following, we will compare the SMB and summer surface energy balance and their components across the main con-
370 tinental scale northern hemisphere ice sheets. We distinguish between six ice sheets: NAISC, GrIS, BKIS, SIS, BIIS and
Icelandic (IcIS). The summer energy balance is analysed to identify the different contributions from incoming solar and long-

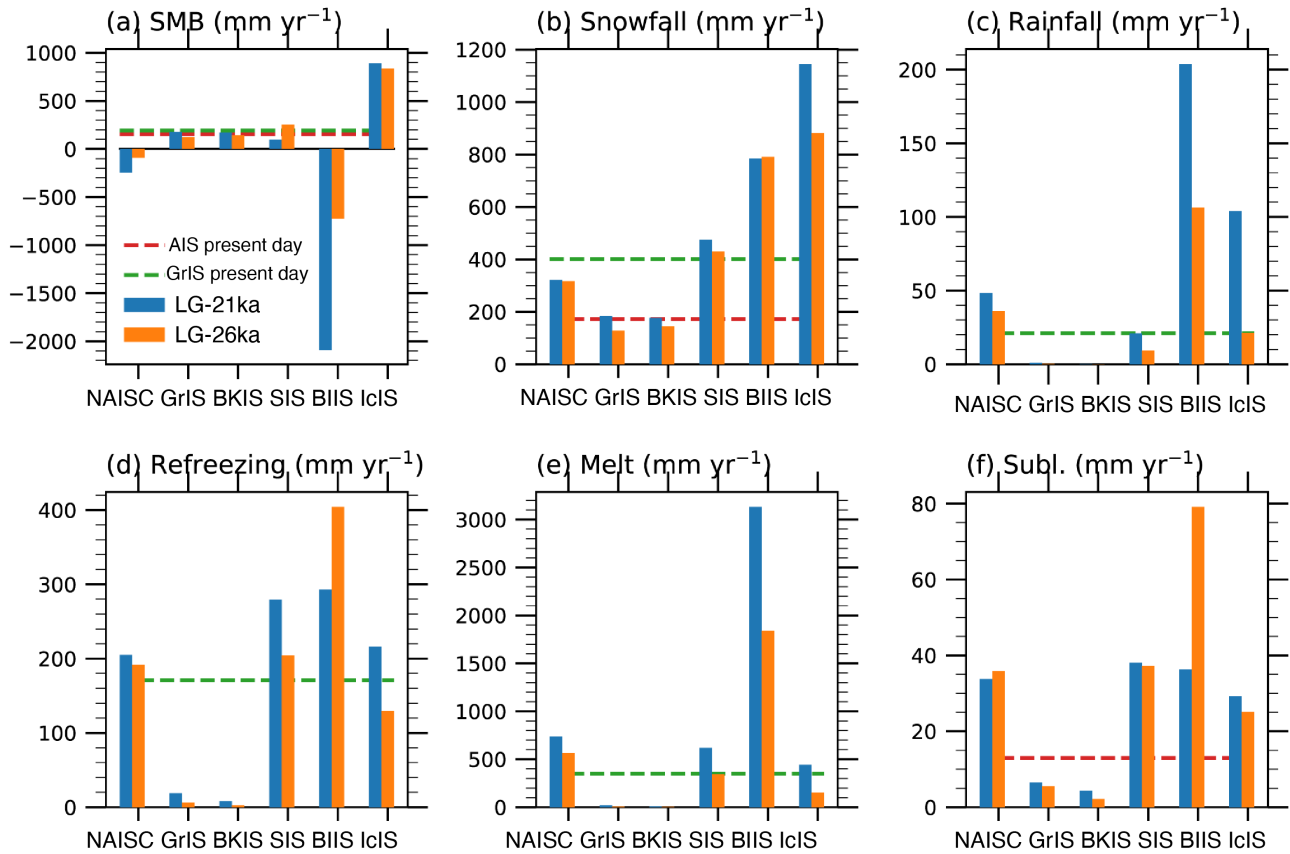


Figure 6. Annual means from the last 20 years of simulation of a) surface mass balance, b) snowfall, c) rainfall, d) refreezing, e) melt, and f) sublimation, all in mm yr^{-1} . Blue bars represent LG-21ka averages while orange bars represent LG-26ka averages, over the individual ice sheets. North American ice sheet complex (Laurentide, Cordilleran and Innuitian (NAISC)), Greenland ice sheet (GrIS), Barents-Kara Sea ice sheet (BKIS), Scandinavian ice sheet (SIS), British-Irish and northsea ice sheet (BIIS), and Icelandic ice sheet (IcIS). The green and red dashed line correspond to present day GrIS and AIS averages (Mottram et al., 2021; Noël et al., 2020). Note the annual means are scaled by ice sheet area (in units of mm yr^{-1}).

wave radiation, albedo and turbulent heat fluxes to melt energy. In the last subsection, we compare the results of LG-26ka and LG-21ka.

4.1 Surface mass balance and components per ice sheet

375 Figure 6 shows a comparison of the spatially-averaged SMB and its components across the six major northern hemisphere ice sheets with the corresponding values for the present-day ice sheets of Greenland (Noël et al., 2020) and Antarctica (Mottram et al., 2021). Average values have been chosen to compare different ice sheets regardless of their different areas.

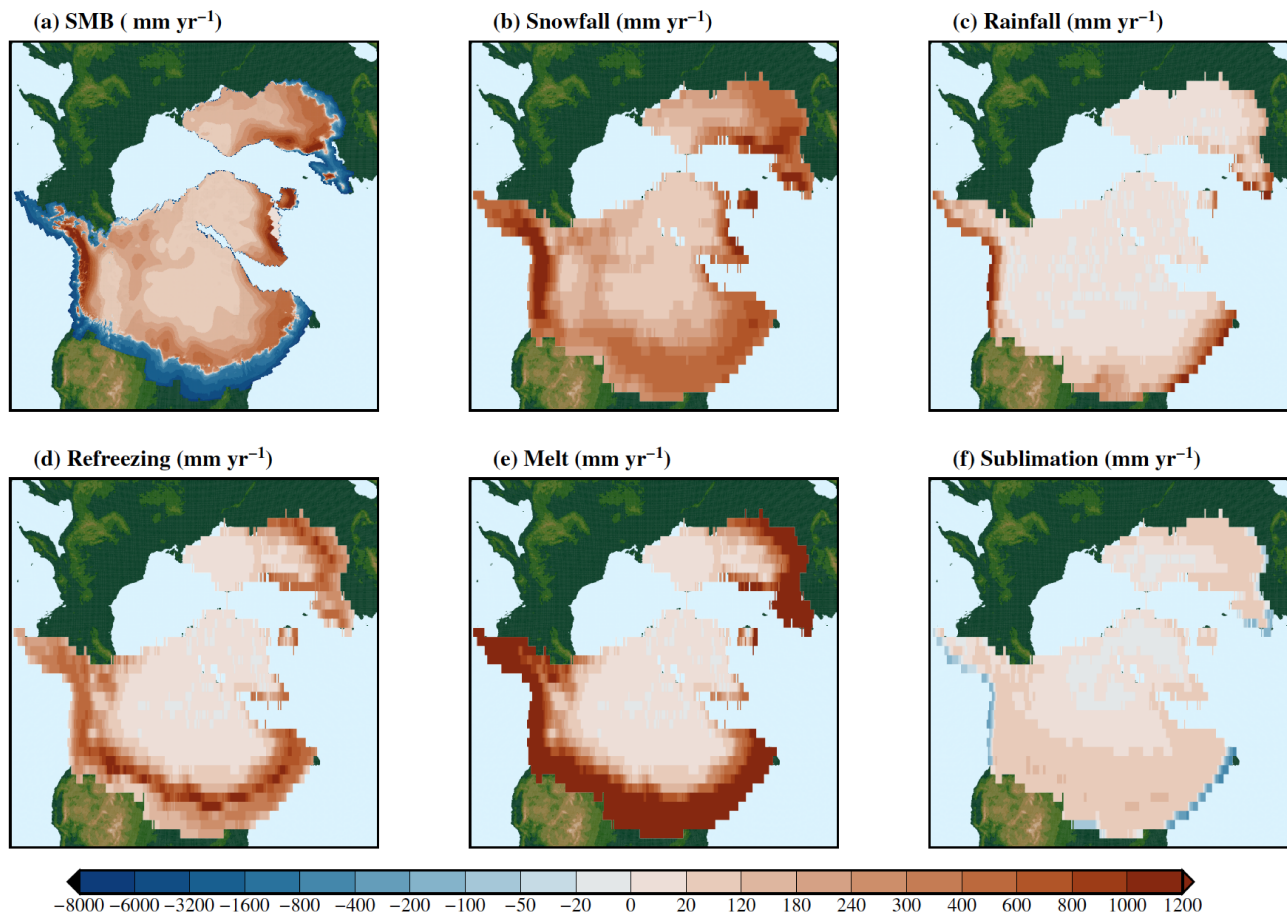


Figure 7. Maps of LG-21ka annual means from the last 20 years of simulation of (a) surface mass balance (downscaled onto the higher resolution CISM2.1 4km grid (A1)), (b) snowfall, (c) rainfall, (d) refreezing, (e) melt, and (f) sublimation, all in mm yr⁻¹.

The averaged SMB of the IcIS, SIS, GrIS and BKIS is positive, with the latter two results of similar value to present-day Greenland and Antarctica (around 200 mm/yr). The similarity in the simulated mean GrIS SMB is the result of the almost zero melt rate (Fig. 6e) at the LGM combined with the 50% reduction in the snowfall rate (200mm/yr at the LGM versus 400 mm/yr for present-day, Fig. 6b). These differences in the SMB components are associated with the colder-lower temperature and drier LGM climate (Fig.?? and Fig.1).

The LG-21ka GrIS excluding the wetter southeast margin (Fig. 7b) and BKIS have similar mean SMB and components: low snowfall rates, zero rainfall and melt (except for a narrow band in southwest Greenland) and interiors with low net snow deposition (Fig. 7b) contrasting with low sublimation-dominated margins (Fig. 7f). All other ice sheets have large areas of melt which largely correspond with the relatively wide ablation areas (Fig. 7a and e). The SIS has a mean SMB that is half of the BKIS, regardless of more than double the snowfall rates (Fig. 6b), with a value very similar to present-day Greenland. This is

due to relatively large melt rates (almost double than for present-day Greenland). The SMB of the IcIS is the largest of all the six ice sheets, due to very high snowfall rate (Fig. 6b) that is only partially compensated by melt rates of a similar magnitude to present-day Greenland.

Two ice sheets have ~~a~~an extremely negative SMB across the ablation area: NAISC and BIIS. The CIS, which is part of the NAISC, has a wide ablation area along the southern and western (Pacific) margins, with the latter corresponding to the high ~~snowfall~~snow accumulation rates over the high elevation of the Sierra Nevada mountain range (Fig. 7b). For the LIS, the high ablation and melt area extends along the entire southern margin, even over the relative high elevation of the southern (Atlantic) margin, due to the relatively ~~warmer~~high (warm) summer temperatures (Fig. C2). High refreezing rates are simulated along the equilibrium line altitude, at the transition between the accumulation and ablation zone along the southern margin (Fig. 7d). Both these ice sheets (CIS and LIS) have high rainfall rates and inverse sublimation (or ~~snowfall~~snow deposition) along the marine terminating margins not bordered by sea ice (see Fig. 2a), with mean values more than double present-day Greenland and Antarctica respectively (Fig. 6c and f). The BIIS has the lowest mean SMB of the six ice sheets, despite ~~of~~ the second largest ~~snowfall accumulation~~after the IcIS snow accumulation. The simulated ablation areas cover most of the ice sheet except for a minimal accumulation area in the interior, across the higher elevation of Scotland (Fig. 7a). The entire ice sheet surface melts seasonally (Fig. 7e), with average melting rates almost an order of magnitude larger than for the present-day Greenland.

If the simulated SMB, including the very wide and negative ablation area of the NAISC and BIIS, was applied to a dynamic ice sheet model (for example, CISM2.1, Lipscomb et al. (2019)) it would be highly unlikely/challenging that the spatial extent of the southern margin in either ice sheet would be maintained; rapid retreat would likely occur. However, as outlined in section 1, the timing of the last glacial maximum for both these ice sheets was earlier than the historical 21 ka BP definition. (25 ka BP for NAISC, 23 ka BP for BIIS). Therefore, an earlier time step in this 6 ka period may be more appropriate to simulate the glacial maximum for these ice sheets. For this reason, in section 4.3, we compare the LG-21ka simulation with LG-26ka.

4.2 Melt sources: the surface energy budget

Here we will examine the components for the summer (JJA) energy budget over all northern hemisphere ice sheets (Fig. 8). Melt is simulated across all margins of the major six continental ice sheets (Fig. 8a) apart from those bordered by sea ice (Fig. 2), for example the BKIS, the eastern margins of GrIS and the arctic sea margin of the LIS.

Incoming solar radiation is high in the interior of the NAISC, GrIS and SIS with much lower rates at the margins (Fig. 8b). Minimum incoming solar radiation is simulated over the southern and Atlantic margins of the NAISC and over the BIIS, due to higher amounts of cloud water over those ablation areas. An increase in shortwave radiation towards the higher elevation in the interior of ice sheets is also a feature of the present-day GrIS (van den Broeke et al., 2008) and is simulated by regional (Ettema et al., 2010) and global climate models (van Kampenhout et al., 2020; Vizcaíno et al., 2013; Dunmire et al., 2022). Conversely, maximum incoming longwave radiation is simulated over the ~~lower, warmer margins of the ice sheets~~margins which have higher temperatures, except for northern North America, GrIS and BKIS (Fig. 8c). Compared to the PI simulation, across the ice sheets there is an increase in cloud fraction (i.e gets cloudier) but the clouds are thinner. These two specific changes in the nature of the clouds can be related to the earlier responses in the radiation fluxes (see Section 3.3). Thinner clouds act to

increase the incoming solar radiation at the surface (Fig.C4a). Conversely, in cloudier areas, the clouds increase the incoming longwave radiation although the clouds are thinner (Fig. C4g,h).

Summer surface albedo (Fig. 8f) is minimum (between 0.5 and 0.55) over the ablation areas corresponding to bare ice exposure. The highest albedo values (>0.80) correspond to dry snow areas extending from northern Canada, where the LIS and ~~HS-Innutian ice sheet (IIS)~~ coalesce, into central and SE Greenland, the ~~IeIS-high-interior-interior of IcIS~~ and most of the BKIS. The combination of this spatial albedo pattern and the reduction in incoming solar radiation over the ablation areas (Fig. 8b), results in maximum net solar radiation over the southern regions of NAISC and SIS ice sheet margins (Fig. 8d). The sensible heat flux (SHF) provides energy for the surface over most of the ablation areas and all over Greenland. The largest flux towards the atmosphere is simulated at intermediate elevations, just above the equilibrium line altitude of the southern half of the NAISC. The latent heat flux (LHF) is positive (directed towards the surface) over a somewhat narrower band than the sensible heat flux along the lowest part of the ablation areas and is negative over the rest of the ice sheets. The positive LHF anomaly along the southern margin of the ice sheets is due to prolonged bare-ice exposure; where when relatively warm and moist air is advected over this region condensation occurs (Sellevold and Vizcaíno, 2020). The ground heat flux (GHF) provides energy to the surface along the areas with maximum refreezing (c.f Fig. 7d and Fig. 8i), due to the heat released in the refreezing process.

4.3 LG-26ka versus LG-21ka surface mass balance

The LG-26ka simulation results in a SMB increase with respect to LG-21ka for the NAISC, BIIS and SIS (Fig. 6 and Fig. 9a), with the largest absolute difference for the BIIS. However, for the NAISC and BIIS this does not reverse the SMB sign, which if applied to an offline ice sheet dynamical model would likely initiate retreat. This increase in the SMB is primarily caused by a reduction in the melt rates (Fig. 6e and Fig. 9e). Over the BIIS, a small increase in snowfall contributes secondarily to higher SMB, and is related to a cooling-related reduced fraction of precipitation falling as rainfall (Fig. 6c and 9b). Gandy et al. (2018) concluded that a warming of the climate after 26 ka, and resultant reduction in SMB was in fact required to initiate the retreat of the BIIS at 21 ka. Therefore, the 1.5°C warming between LG-26ka and LG-21ka due to the change in orbital parameters may be one factor that led to the retreat of the BIIS, due to the increase in melt rate (Fig.6e).

Over the other five ice sheets, snowfall rates are lower in the LG-26ka simulation compared with LG-21ka. Mean rainfall rates decrease over all ice sheets, apart from the two driest (GrIS and BKIS) where it remains almost zero. The largest reduction is over the ice sheets with a prominent North Atlantic climate (BIIS and IcIS).

The SMB is lower in LG-26ka with respect to LG-21ka for the two ice sheets with almost zero melt (GrIS and BKIS) and the IcIS, that has relatively low average melt rates. This decrease is due to reduced snowfall (Fig. 6b). A fall in melt rates at LG-26ka results in a refreezing reduction over all ice sheets except for the BIIS, where the combination of a large reduction in melt and rainfall and a minor increase in precipitation results in an increase in refreezing (Fig. 6d and Fig. 9d). Spatially (Fig. 9a), the SMB increases over the ablation areas and decreases in the accumulation areas, the latter due to reductions in snowfall (Fig. 9b). Snowfall increases and rainfall decreases along the western margin of the NAISC, in connection with colder

455 [\(lower\)](#) temperatures (Fig. 1b). Refreezing increases over the ablation areas, in connection with a cooling-induced increase in the refreezing capacity, and decreases over the percolation areas, as a result of the reduction in melt (Fig. 9d and e).

5 Discussion and conclusions

Here, we present for the first time a detailed, explicit analysis of climate, SMB and energy components over northern hemisphere ice sheets, with a similar approach as adopted for modern ice sheets with regional climate models (Ettema et al., 2010, 2009; Noël et al., 2018, 2020) and projections with global climate models (Muntjewerf et al., 2020a). This detailed analysis of surface mass and energy components is meant to facilitate an advanced comparison of climate and ice sheet simulations between (multiple) past and future time periods. A direct evaluation of our simulated SMB and components is not straightforward as there are no direct proxies available for the LGM, except for ~~snowfall~~-[snow](#) accumulation rates over the GrIS. Therefore, here we will briefly compare our results with Kapsch et al. (2021), who presented results of the spatial distribution of the SMB of the Northern Hemisphere ice sheets during the last deglaciation. In their study, they downscale their results to two different ice sheet reconstructions; ICE6G (Peltier et al., 2015) and GLAC1D (Tarasov et al., 2012). Our simulated LG-21ka SMB spatial distribution is largely similar to Kapsch et al. (2021) downscaled onto the GLAC1D topography (this topography is the same for the NAISC in both studies) (Fig. 7 and Kapsch et al. (2021) figure 4). The simulation over common accumulation areas is very similar, with precipitation maxima over the CIS and southwestern Laurentide and southern Scandinavian, and minima over present-day Hudson Bay, northern half of Greenland and the BKIS. The width of our ablation areas is difficult to compare as we present results on the climate (land component) grid while Kapsch et al. (2021) are on a higher resolution grid. However, in general the distribution of ablation areas is very similar, with the major discrepancy being we have a larger ablation area for the BIIS that in their case. This discrepancy is smaller if we compare with their SMB downscaled to the ICE6G reconstruction (their Figure A2). For the Scandinavian and BKIS, our ablation area simulation is closest to Kapsch et al. (2021) downscaled to the GLAC-1D topography.

Our simulated SMB for the NAISC [and BIIS](#) appears too negative to prevent large marginal retreat if used as forcing for an ice sheet dynamical model. This suggests that one or more of this could explain this low SMB: a) biases in the climate and/or snow/firn simulation, b) biases in the ice sheet reconstruction (as the SMB is largely dependent on surface topography), c) climate and SMB conditions largely out of equilibrium during the LGM. ~~In following work, we will apply the simulated SMB as forcing for an ice sheet model to simulate ice sheet flow during the LGM~~ [A recent study by Gandy et al. \(2023\) also investigated the LGM NAISC in a coupled climate ice sheet model 'FAMOUS-ice'. This study found that when initiating their simulations from a large NAISC \(as adopted in this study\), a large ablation area formed across the southern margin of ice sheet, which led to rapid ice sheet retreat \(see Fig.3 in Gandy et al. \(2023\)\). This behaviour was attributed to the heavy tuning of their model to present-day Greenland. As CESMv2.1 model has also been shown to have problems when applied the LGM climate \(Zhu et al., 2021\) and required de-tuning to comply with LGM GMST constraints. Future work investigating coupled ice sheet-climate simulation for the LGM with CESMv2.1 may also require de-tuning to correctly simulate the LGM North Hemisphere ice sheets.](#)

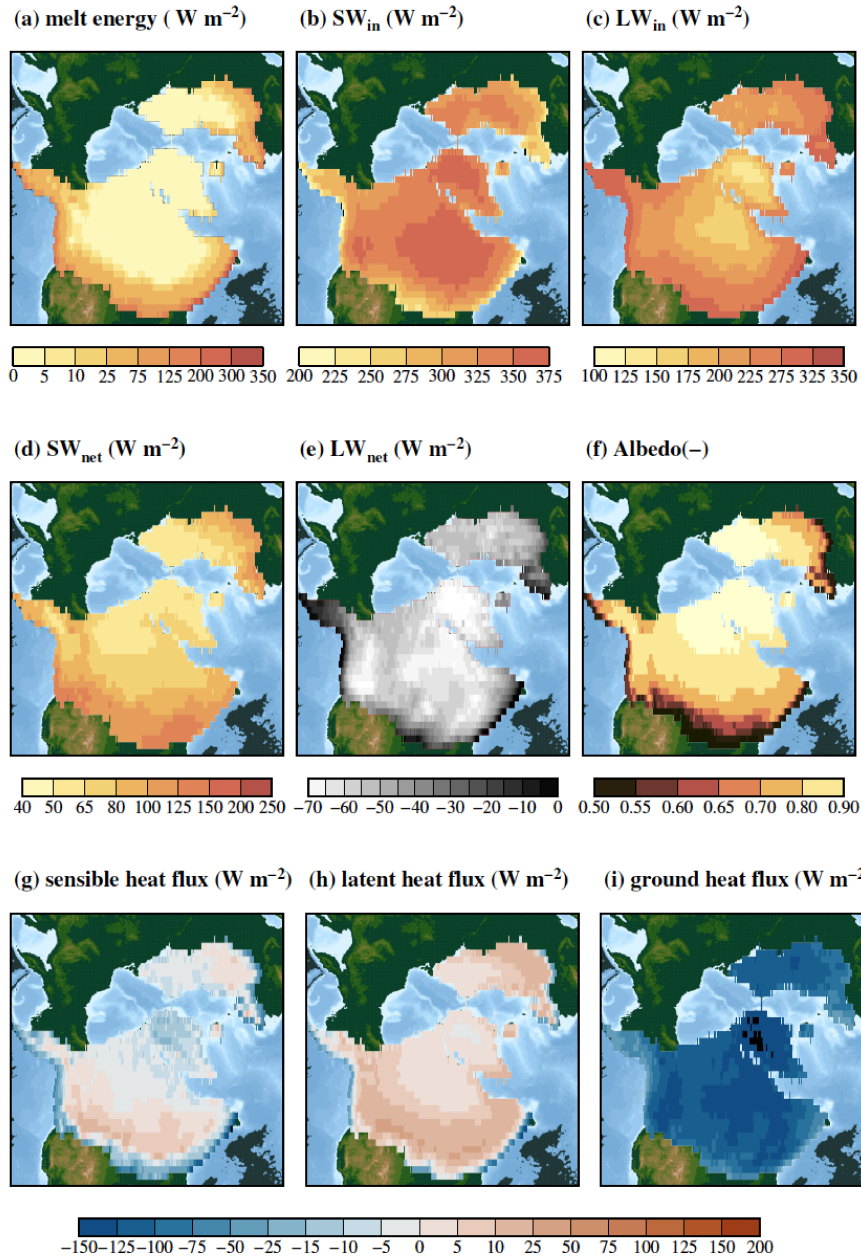


Figure 8. Maps of LG-21ka summer (JJA) means from the last 20 years of simulation of (a) melt energy (ME) ($W m^{-2}$), (b) SW_{in} ($W m^{-2}$), (c) LW_{in} ($W m^{-2}$), (d) SW_{net} ($W m^{-2}$), (e) LW_{net} ($W m^{-2}$), (f) albedo (-), (g) sensible heat flux (SHF) ($W m^{-2}$), (h) latent heat flux (LHF) ($W m^{-2}$), and (i) ground heat flux (GHF) ($W m^{-2}$).

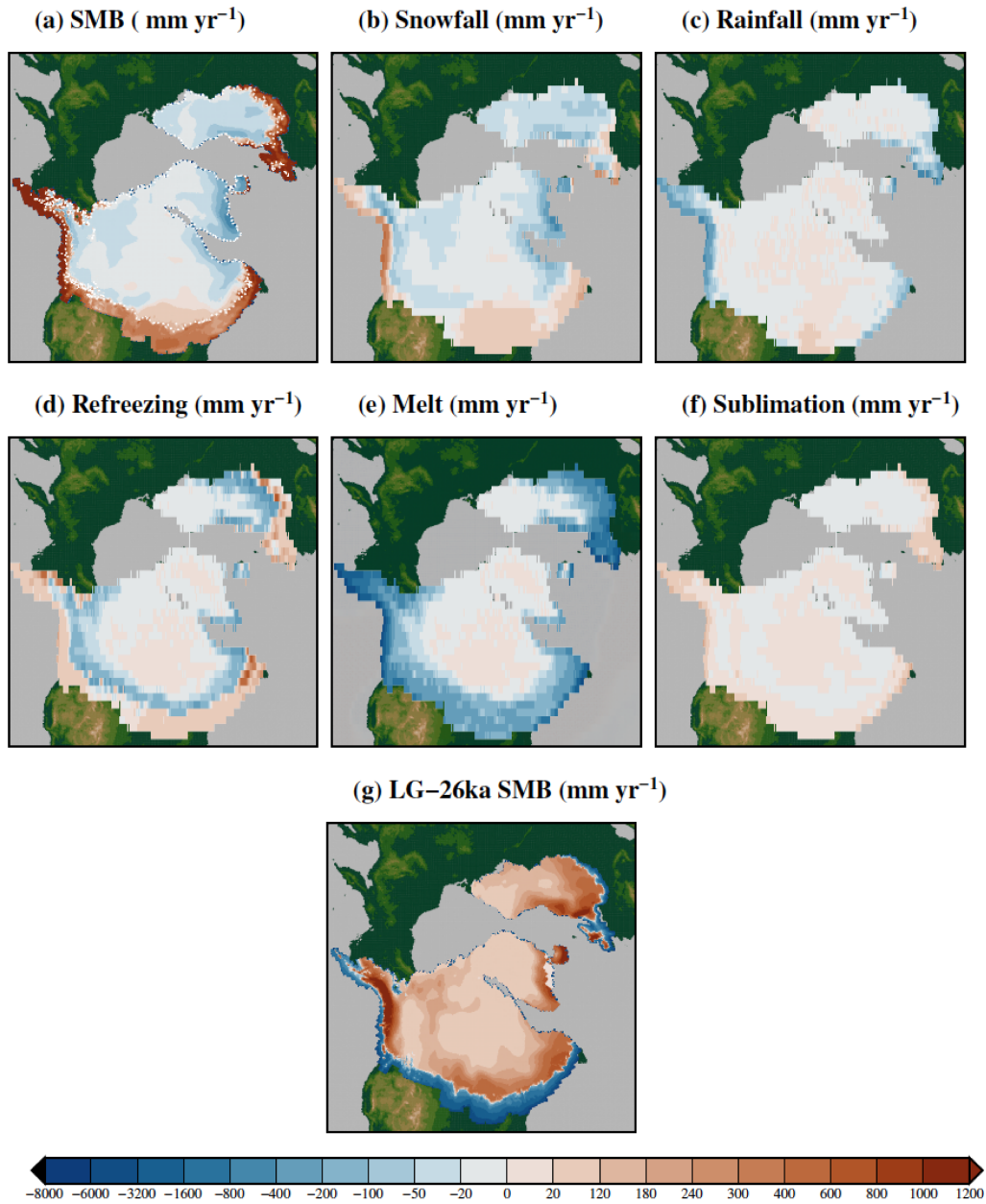


Figure 9. Difference between the results of the LG-26ka and LG-21ka (annual means from the last 20 years of each simulation). (a) surface mass balance, (b) snowfall, (c) rainfall, (d) refreezing, (e) melt, and (f) sublimation, all in mm yr^{-1} . (g) [surface mass balance for LG-26ka \(downscaled onto the higher resolution CISM2.1 4km grid \(A1\)\)](#)

Code availability. TEXT

Data availability. The Osman et al. (2021) data was downloaded from: <https://www.ncdc.noaa.gov/paleo/study/33112>. The Paul et al. (2021) 490 was downloaded from: <https://doi.org/10.1594/PANGAEA.923262>

Appendix A: Ice sheet reconstruction

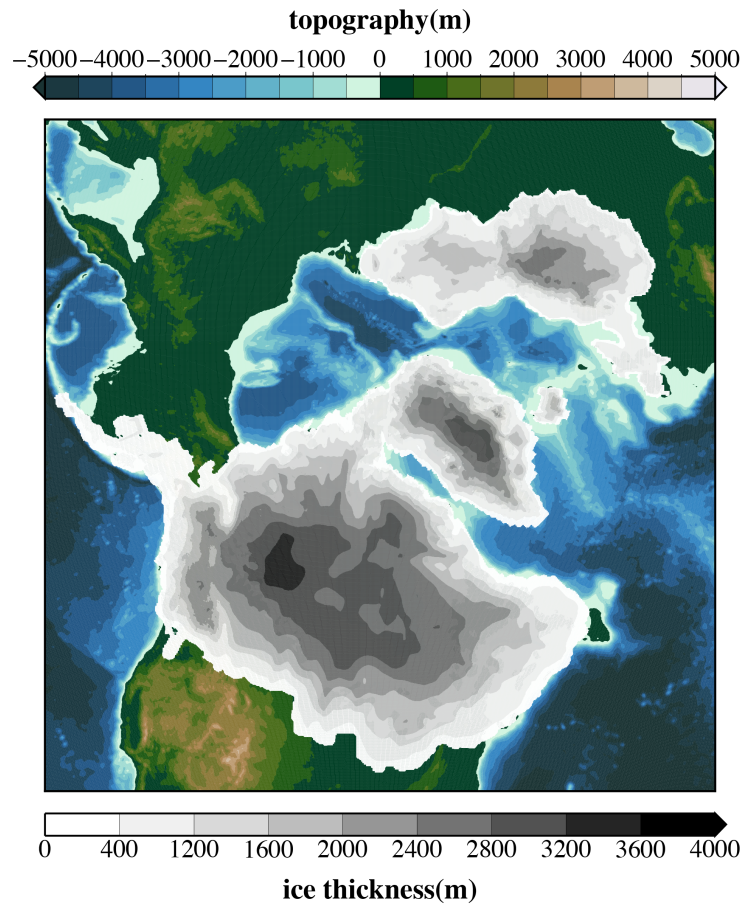


Figure A1. Ice sheet reconstructions used for simulations LG-21ka and LG-26ka at the finer CISM2.1 grid that is used for the elevation classes calculation of the surface mass balance. The reconstruction combines the Antarctic and Patagonia ice sheets from ICE5G (Peltier, 2004), the North American ice sheet complex (Laurentide, Cordilleran and Innuitian) (Tarasov et al., 2012), Greenland ice sheet (Lecavalier et al., 2014) and the Eurasian ice sheet complex (British and Irish, Scandinavian and Barents-Kara Sea) from BRITICE-CHRONO (Clark et al., 2021)

Appendix B: Generation of input paleovegetation dataset

An offline vegetation model (BIOME4, <https://github.com/jedokaplan/BIOME4>, Kaplan et al. (2003)) was ran using climate forcing of LG-21ka simulation to generate a LGM vegetation distribution. This simulated LGM vegetation distribution was
495 combined with a present-day vegetation dataset as follows:

- The CLM5 standard present-day vegetation dataset Lawrence et al. (2019) is prescribed over the Southern Hemisphere and at low latitudes in the Northern Hemisphere. In these locations, the present-day vegetation is extrapolated over LGM emerged land using a nearest-neighbor mapping algorithm.
- At higher latitudes in the Northern Hemisphere (North of 35 N in Europe and Asia, North of 20 N in North America) we
500 prescribe a LGM vegetation based on the BIOME4 stand-alone simulation, which is run on a 0.5-degree global grid, and is forced with:
 - monthly-averaged [surface-2 m](#) temperature, precipitation and cloudiness for the last 20 years of a 90 years-long CESM2 LGM simulation using the standard present-day vegetation dataset;
 - LGM CO₂, and orbitals (as in the CESM2 LGM simulation 21ka);
 - 505 – LGM soil properties dataset, provided as a personal communication by J. Kaplan.

The LGM BIOME4-simulated vegetation types are converted into CLM5 Plant Functional Types (PFTs) following the conversion table 2.1 in Oleson et al. (2013). Moreover, the following additional corrections are applied:

- Boreal broadleaf deciduous shrubs and boreal grass are prescribed over the Siberian continental shelf;
 - Tropical broadleaf evergreen trees north of 20 N have been converted to temperate broadleaf evergreen trees.
- 510 In Fig. B1, we show maps of the PFT percentage in the hybrid LGM/present-day vegetation dataset, whereas in Fig. B2 we show the output of the LGM BIOME4 simulation.

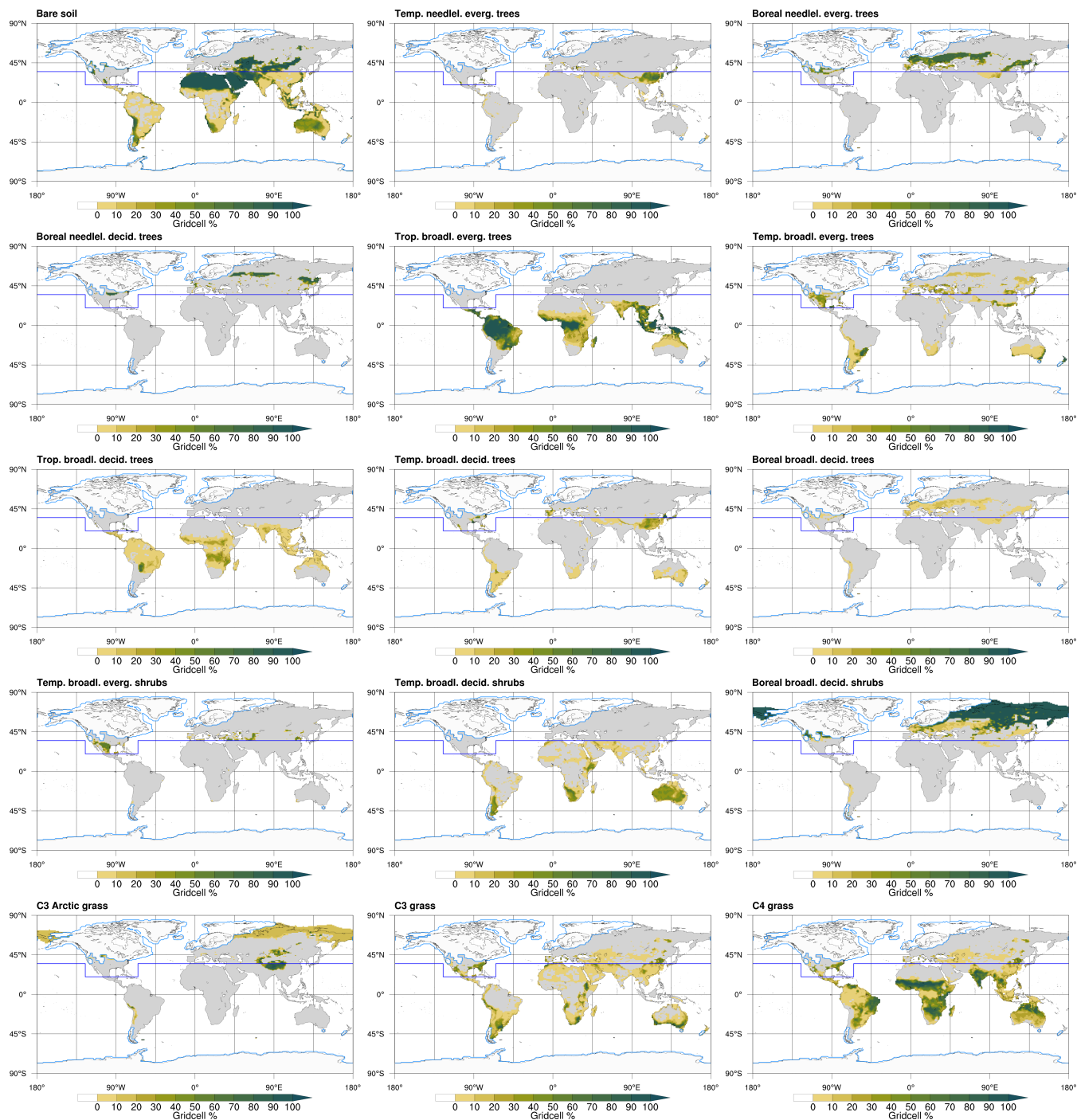


Figure B1. Global map of percentage of land cover, for each CLM5 Plant Functional Type (PFT), in the hybrid LGM/present-day vegetation dataset. The dark blue line indicates the latitude limit above which the LGM BIOME4-based vegetation is used, instead of the standard CLM5 present-day vegetation dataset (which is prescribed below the latitude limit).

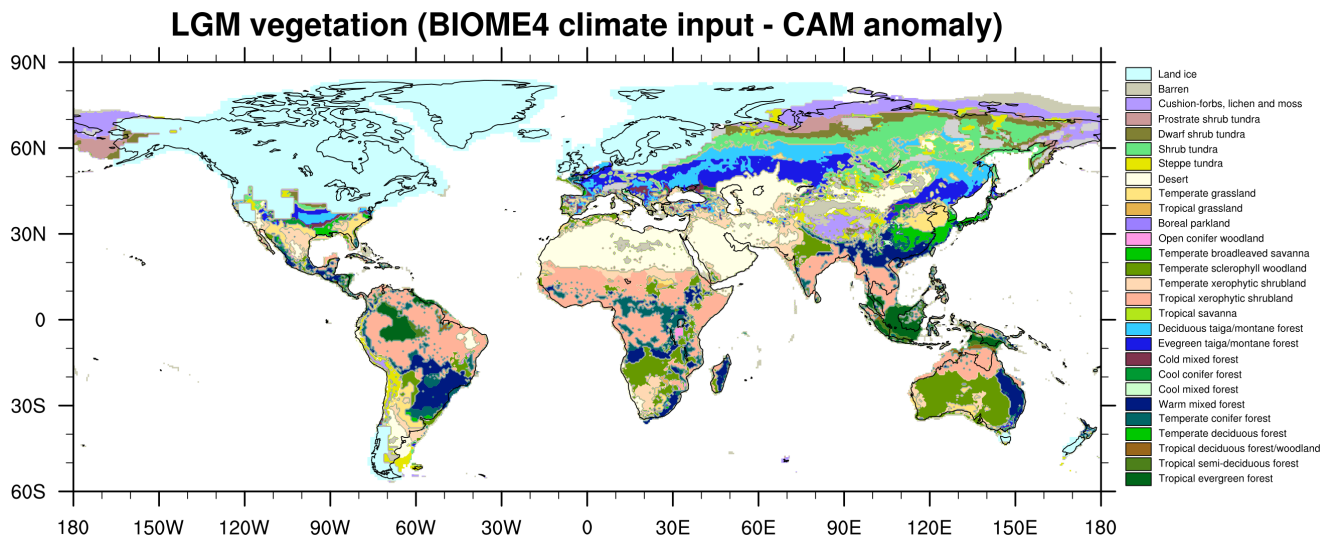


Figure B2. Simulated vegetation types in the BIOME4 stand-alone simulation.

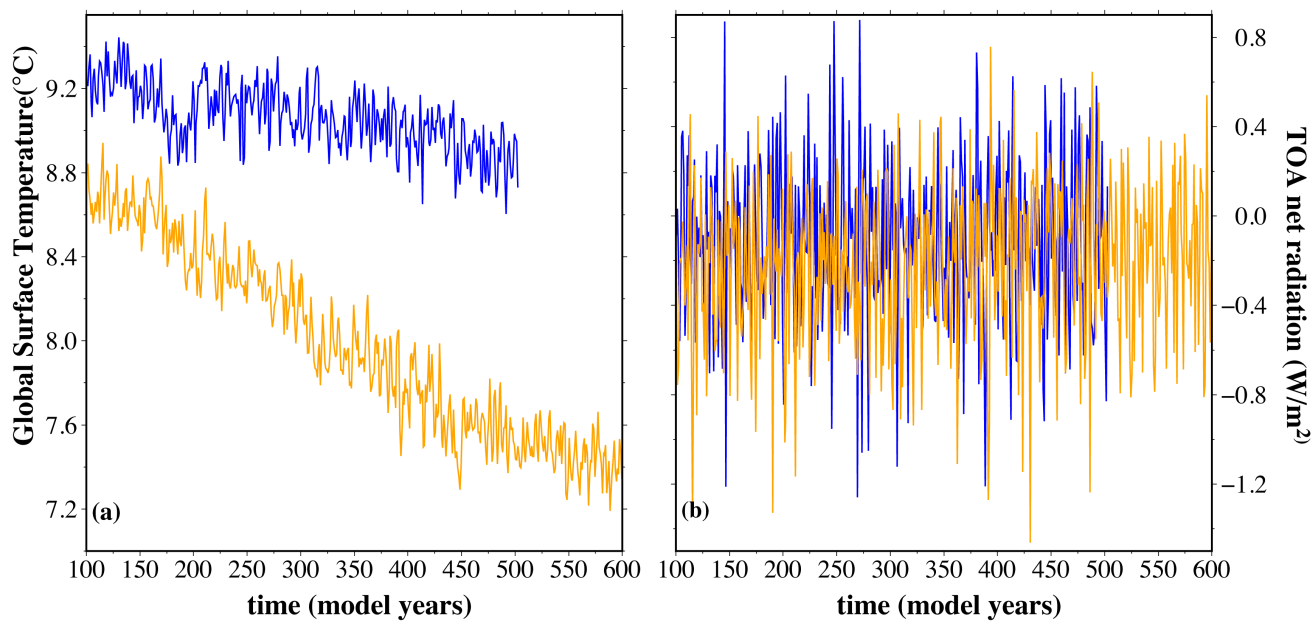


Figure C1. (a) Global surface-near-surface temperature ($^{\circ}\text{C}$) from LG-21ka (blue line) and LG-26ka (orange line). (b) Top of the atmosphere (TOA) net radiation (W/m^2) for LG-21ka (blue line) and LG-26ka (orange line)

Appendix C: Simulated climate

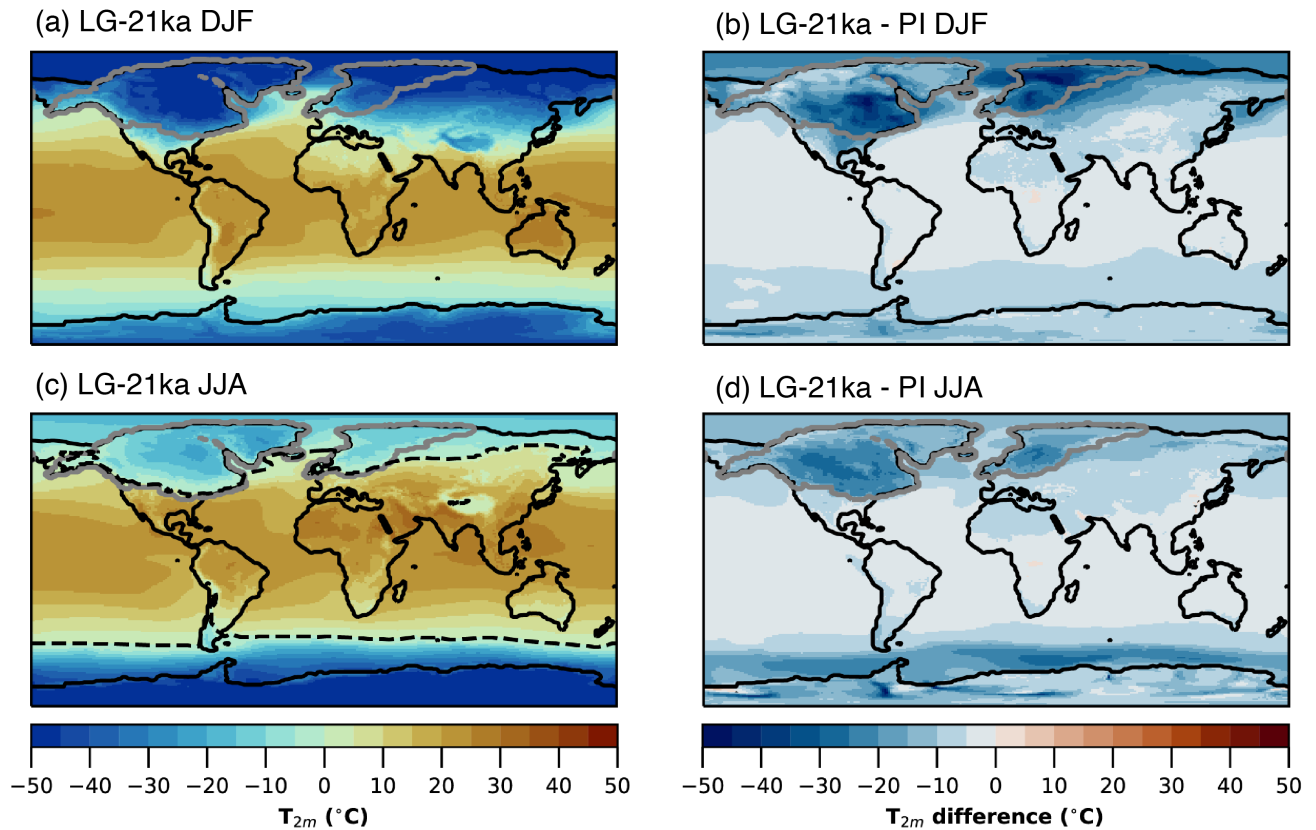


Figure C2. Near-surface temperature. a) and b) shows for DJF, while c) and d) shows for JJA, all in $^{\circ}\text{C}$. The left column shows values from the LG-21ka simulation, while the right column shows the differences between LG-21ka and the PI simulations. Grey contour encloses glaciated areas (>50% ice cover). The black dashed line in c) follows the 0°C isotherms

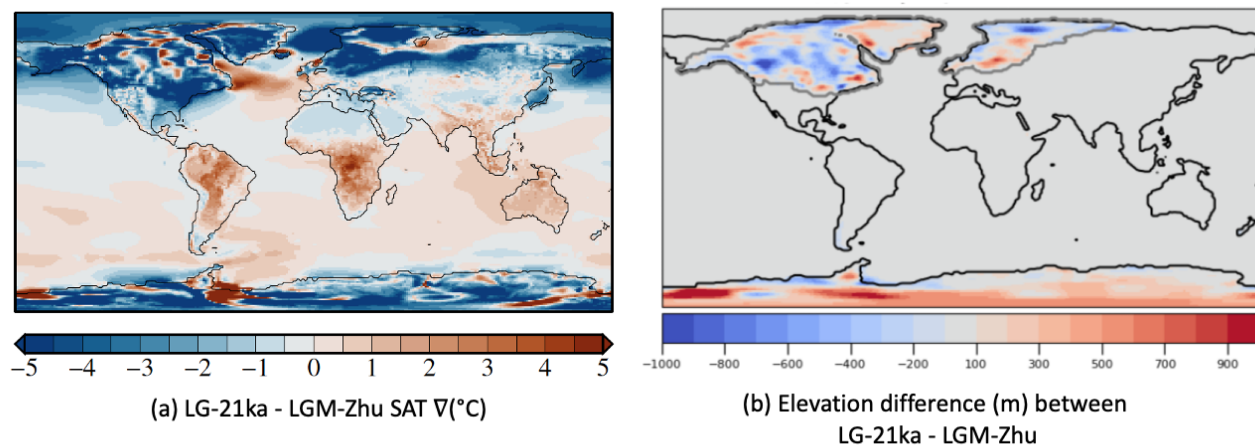


Figure C3. (a) Difference in the annual mean (20 years) near-surface temperature (SAT) between LG-21ka and LGM-Zhu. (b) Elevation difference (m) in CAM (1 $^{\circ}$ CESM grid) between LG-21ka and LGM-Zhu. There is an approximate relationship between colder region (blue) in (a) and the higher elevations in (b).

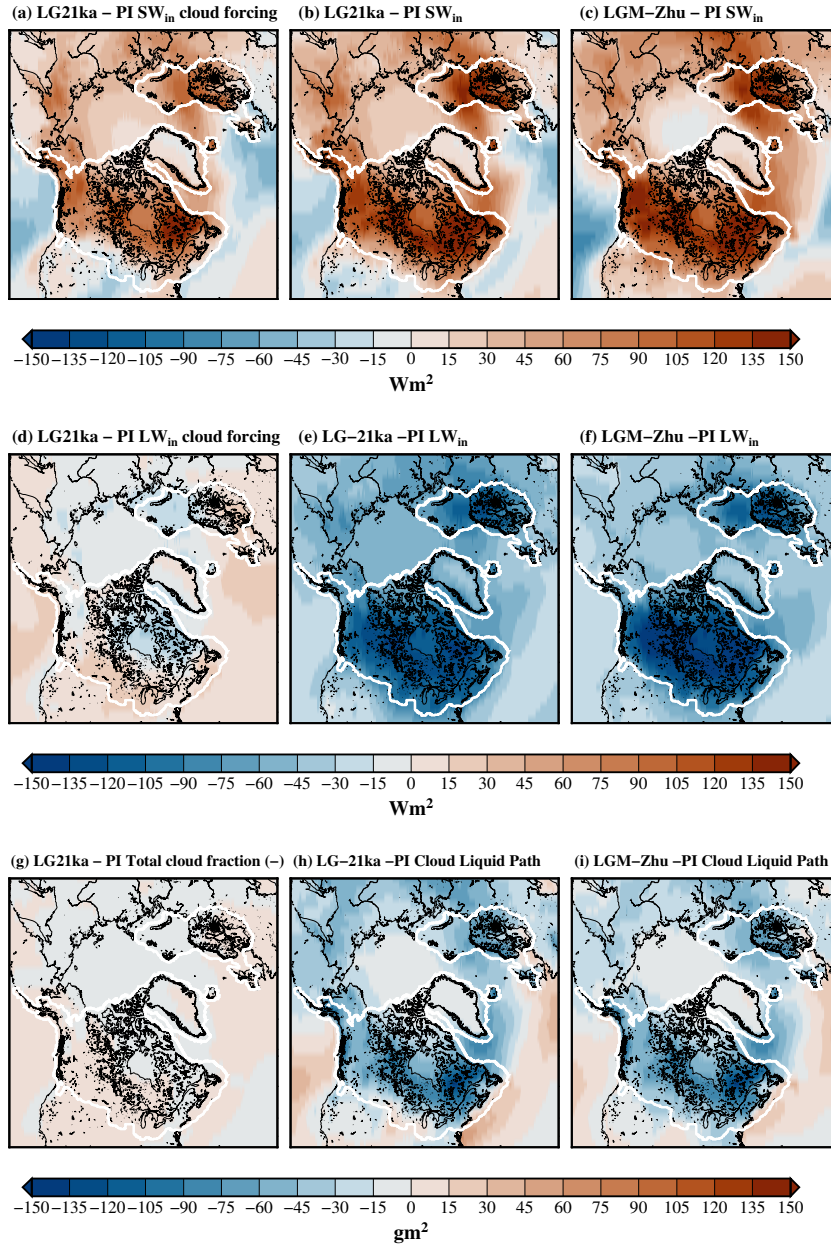


Figure C4. JJA (June, July, Aug) anomalies (relative to PI) for (a) LG-21ka SW_{in} cloud forcing , (b) LG-21ka SW_{in} , (c) LGM-Zhu(SW_{in}), (d) LG-21ka LW_{in} cloud forcing , (e) LG-21ka LW_{in} , (f) LGM-Zhu LW_{in} , (g) LG-21katotal cloud fraction (-), (h) LG-21kaCloud liquid path and (i) LGM-ZhuCloud liquid path.

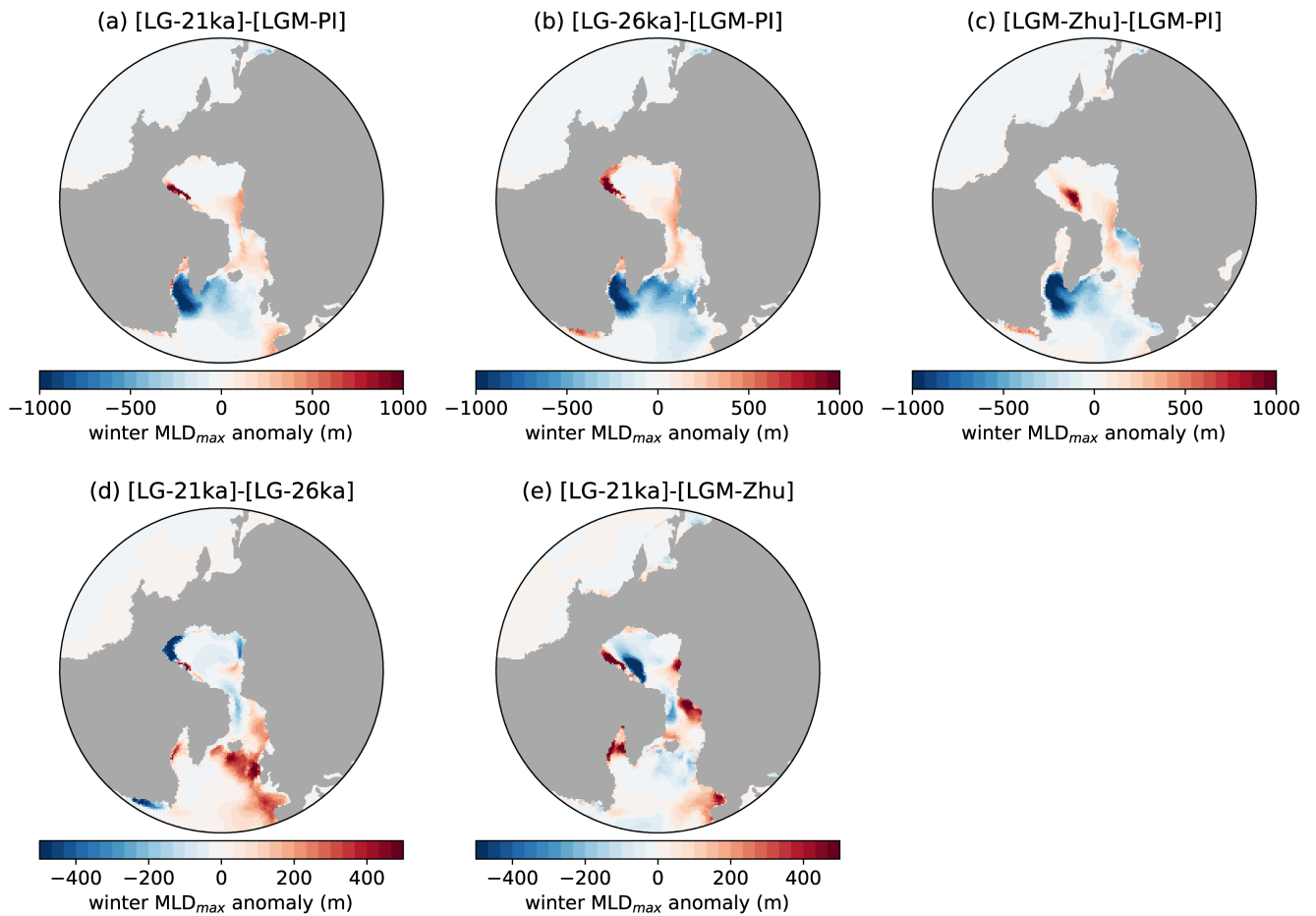


Figure C5. Anomaly of the local maximum of the mixed layer depth during wintertime (in m) for (a) LG-21ka, (b) LG-26ka and (c) LGM-Zhu with respect to the LGM-PI simulation and for LG-21ka with respect to (d) LG-26ka and (e) LGM-Zhu.

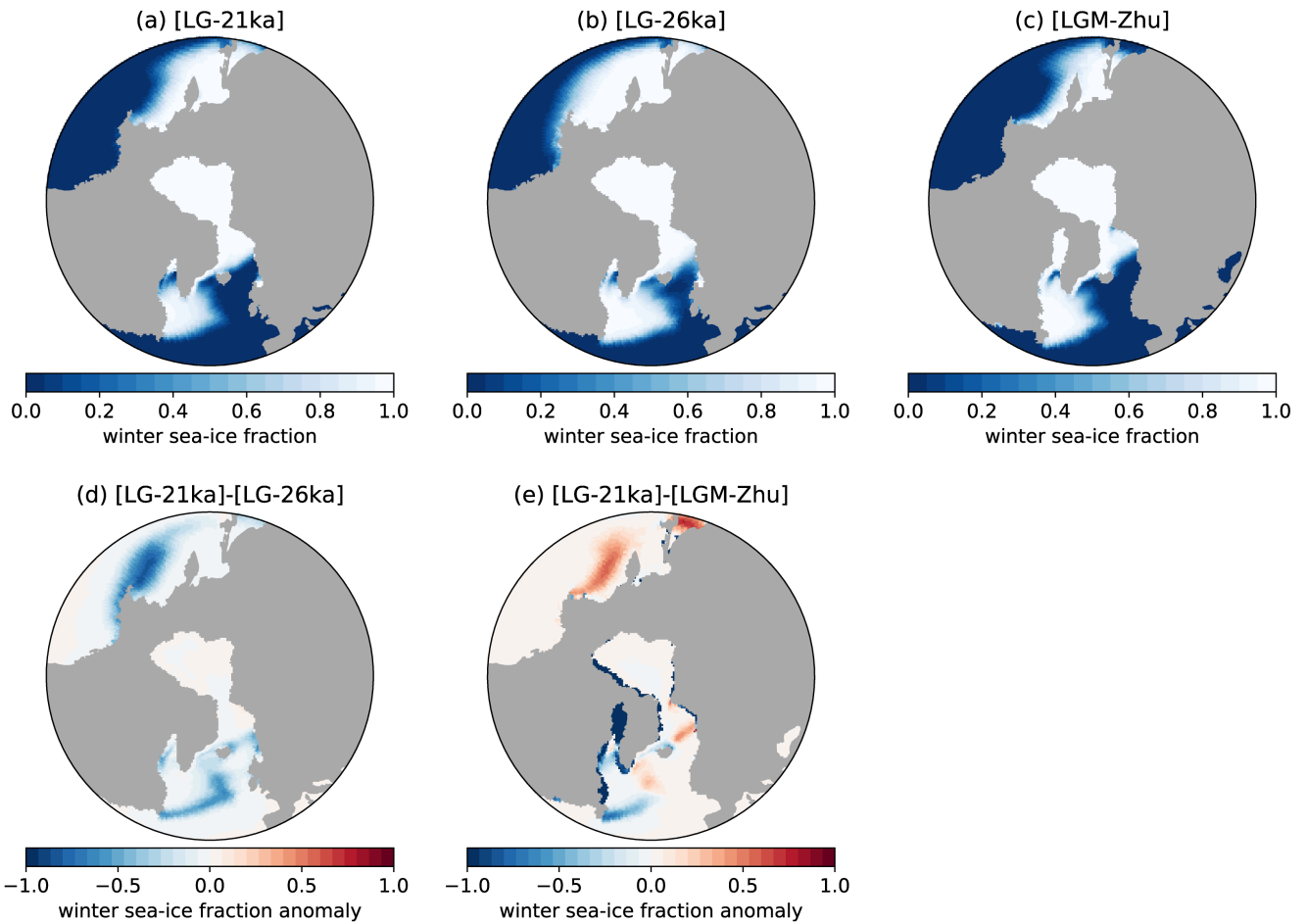


Figure C6. Sea ice fraction during wintertime for (a) LG-21ka, (b) LG-26ka and (c) LGM-Zhu. Winter sea ice fraction anomaly for LG-21ka with respect to (d) LG-26ka and (e) LGM-Zhu.

Author contributions. SB and MP designed the simulations and prepared initial and boundary conditions, SB and RS ran the simulations. RS, SB and SG analysed the simulated climate, RS and MV analysed the simulated SMB. JZ and BOB assessed modelling choices as the
515 choice of CAM5 over CAM6. ML provided model grids. SB, RS, SG, MP and MV wrote the manuscript. MV supervised the project and SB coordinated the writing of the manuscript. All authors read the text and provided comments.

Competing interests. The authors declare that there are no competing interests

Acknowledgements. R.S., M.P., M.V. and S.G. acknowledge funding from the ERC Starting Grant CoupledIceClim 678145. S.L.B. has received support from the European Research Council (ERC) under the European Union's Horizon 2020 research and innovation programme
520 (ERC Advanced Grant PALGLAC 787263). The CESM project is supported primarily by the National Science Foundation (NSF). This material is based upon work supported by the National Center for Atmospheric Research, which is a major facility sponsored by the NSF under Cooperative Agreement No. 1852977. The authors thank J. Kaplan for providing the LGM soil properties dataset and for his suggestions on the setup of the BIOME4 LGM vegetation simulation.

References

- 525 Bereiter, B., Sarah, E., Jochen, S., Christoph, N.-A., F., S. T., Hubertus, F., Sepp, K., and Jerome, C.: Revision of the EPICA Dome C CO₂ record from 800 to 600 kyr before present, *Geophysical Research Letters*, 42, 542–549, <https://doi.org/https://doi.org/10.1002/2014GL061957>, 2015.
- Berger, A.: Long-Term Variations of Daily Insolation and Quaternary Climatic Changes, *Journal of Atmospheric Sciences*, 35, 2362–2367, [https://doi.org/10.1175/1520-0469\(1978\)035<2362:LTVODI>2.0.CO;2](https://doi.org/10.1175/1520-0469(1978)035<2362:LTVODI>2.0.CO;2), 1978.
- 530 Brady, E. C., Otto-Bliesner, B. L., Kay, J. E., and Rosenbloom, N.: Sensitivity to Glacial Forcing in the CCSM4, *Journal of Climate*, 26, 1901 – 1925, <https://doi.org/10.1175/JCLI-D-11-00416.1>, 2013.
- Clark, C. D., Chiverrell, R. C., Fabel, D., Hindmarsh, R. C. A., Ó Cofaigh, C., and Scourse, J. D.: Timing, pace and controls on ice sheet retreat: an introduction to the BRITICE-CHRONO transect reconstructions of the British–Irish Ice Sheet, *Journal of Quaternary Science*, 36, 673–680, <https://doi.org/https://doi.org/10.1002/jqs.3326>, <https://doi.org/10.1002/jqs.3326>, 2021.
- 535 Clark, C. D., Ely, J. C., Hindmarsh, R. C. A., Bradley, S., Ignéczi, A., Fabel, D., Ó Cofaigh, C., Chiverrell, R. C., Scourse, J., Benetti, S., Bradwell, T., Evans, D. J. A., Roberts, D. H., Burke, M., Callard, S. L., Medialdea, A., Saher, M., Small, D., Smedley, R. K., Gasson, E., Gregoire, L., Gandy, N., Hughes, A. L. C., Ballantyne, C., Bateman, M. D., Bigg, G. R., Doole, J., Dove, D., Duller, G. A. T., Jenkins, G. T. H., Livingstone, S. L., McCarron, S., Moreton, S., Pollard, D., Praeg, D., Sejrup, H. P., Van Landeghem, K. J. J., and Wilson, P.: Growth and retreat of the last British–Irish Ice Sheet, 31 000 to 15 000 years ago: the BRITICE-CHRONO reconstruction, *Boreas*, 51, 699–758, <https://doi.org/https://doi.org/10.1111/bor.12594>, 2022.
- 540 Clark, P. U., Dyke, A. S., Shakun, J. D., Carlson, A. E., Clark, J., Wohlfart, h. B., Mitrovica, J. X., Hostetler, S. W., and McCabe, A. M.: The Last Glacial Maximum, *Science*, 325, 710–714, <https://doi.org/10.1126/science.1172873>, doi: 10.1126/science.1172873, 2009.
- Dalton, A. S., Stokes, C. R., and Batchelor, C. L.: Evolution of the Laurentide and Innuitian ice sheets prior to the Last Glacial Maximum (115 ka to 25 ka), *Earth-Science Reviews*, 224, 103 875, <https://doi.org/https://doi.org/10.1016/j.earscirev.2021.103875>, 2022.
- 545 Danabasoglu, G., G., L. W., and P., B. B.: Climate impacts of parameterized Nordic Sea overflows, *Journal of Geophysical Research: Oceans*, 115, <https://doi.org/https://doi.org/10.1029/2010JC006243>, 2010.
- Danabasoglu, G., Lamarque, J. F., Bacmeister, J., Bailey, D. A., DuVivier, A. K., Edwards, J., Emmons, L. K., Fasullo, J., Garcia, R., Gettelman, A., Hannay, C., Holland, M. M., Large, W. G., Lauritzen, P. H., Lawrence, D. M., Lenaerts, J. T. M., Lindsay, K., Lipscomb, W. H., Mills, M. J., Neale, R., Oleson, K. W., Otto-Bliesner, B., Phillips, A. S., Sacks, W., Tilmes, S., van Kampenhout, L., Vertenstein, M., Bertini, A., Dennis, J., Deser, C., Fischer, C., Fox-Kemper, B., Kay, J. E., Kinnison, D., Kushner, P. J., Larson, V. E., Long, M. C., Mickelson, S., Moore, J. K., Nienhouse, E., Polvani, L., Rasch, P. J., and Strand, W. G.: The Community Earth System Model Version 2 (CESM2), *Journal of Advances in Modeling Earth Systems*, 12, e2019MS001 916, <https://doi.org/https://doi.org/10.1029/2019MS001916>, 2020.
- 550 DiNezio, P. N., Tierney, J. E., Otto-Bliesner, B. L., Timmermann, A., Bhattacharya, T., Rosenbloom, N., and Brady, E.: Glacial changes in tropical climate amplified by the Indian Ocean, *Science Advances*, 4, eaat9658, <https://doi.org/10.1126/sciadv.aat9658>, 2018.
- Dunmire, D., Lenaerts, J. T. M., Datta, R. T., and Gorte, T.: Antarctic surface climate and surface mass balance in the Community Earth System Model version 2 during the satellite era and into the future (1979–2100), *The Cryosphere*, 16, 4163–4184, <https://doi.org/10.5194/tc-16-4163-2022>, 2022.

- Ettema, J., van den Broeke, M. R., van Meijgaard, E., van de Berg, W. J., Bamber, J. L., Box, J. E., and Bales, R. C.: Higher surface mass balance of the Greenland ice sheet revealed by high-resolution climate modeling, *Geophysical Research Letters*, 36, <https://doi.org/https://doi.org/10.1029/2009GL038110>, 2009.
- Ettema, J., van den Broeke, M. R., van Meijgaard, E., and van de Berg, W. J.: Climate of the Greenland ice sheet using a high-resolution climate model – Part 2: Near-surface climate and energy balance, *The Cryosphere*, 4, 529–544, <https://doi.org/10.5194/tc-4-529-2010>, 2010.
- 565 Fyke, J., Sergienko, O., Lofverstrom, M., Price, S., and Lenaerts, J. T. M.: An Overview of Interactions and Feedbacks Between Ice Sheets and the Earth System, *Reviews of Geophysics*, 56, 361–408, <https://doi.org/https://doi.org/10.1029/2018RG000600>, 2018.
- Gandy, N., Gregoire, L. J., Ely, J. C., Clark, C. D., Hodgson, D. M., Lee, V., Bradwell, T., and Ivanovic, R. F.: Marine ice sheet instability and ice shelf buttressing of the Minch Ice Stream, northwest Scotland, *The Cryosphere*, 12, 3635–3651, <https://doi.org/10.5194/tc-12-3635-2018>, 2018.
- 570 Gandy, N., Astfalck, L. C., Gregoire, L. J., Ivanovic, R. F., Patterson, V. L., Sherriff-Tadano, S., Smith, R. S., Williamson, D., and Rigby, R.: De-Tuning Albedo Parameters in a Coupled Climate Ice Sheet Model to Simulate the North American Ice Sheet at the Last Glacial Maximum, *Journal of Geophysical Research: Earth Surface*, 128, e2023JF007250, <https://doi.org/https://doi.org/10.1029/2023JF007250>, e2023JF007250 2023JF007250, 2023.
- Gottelman, A., Hannay, C., Bacmeister, J. T., Neale, R. B., Pendergrass, A. G., Danabasoglu, G., Lamarque, J.-F., Fasullo, J. T., Bailey, D. A., Lawrence, D. M., and Mills, M. J.: High Climate Sensitivity in the Community Earth System Model Version 2 (CESM2), *Geophysical Research Letters*, 46, 8329–8337, <https://doi.org/https://doi.org/10.1029/2019GL083978>, 2019.
- 575 Gu, S., Liu, Z., Oppo, D. W., Lynch-Stieglitz, J., Jahn, A., Zhang, J., and Wu, L.: Assessing the potential capability of reconstructing glacial Atlantic water masses and AMOC using multiple proxies in CESM, *Earth and Planetary Science Letters*, 541, <https://doi.org/10.1016/j.epsl.2020.116294>, 2020.
- 580 Hughes, A. L. C., Richard, G., Øystein S., L., Jan, M., and Inge, S. J.: The last Eurasian ice sheets – a chronological database and time-slice reconstruction, *DATED-1, Boreas*, 45, 1–45, <https://doi.org/https://doi.org/10.1111/bor.12142>, 2016.
- Hurrell, J. W., Holland, M. M., Gent, P. R., Ghan, S., Kay, J. E., Kushner, P. J., Lamarque, J.-F., Large, W. G., Lawrence, D., Lindsay, K., Lipscomb, W. H., Long, M. C., Mahowald, N., Marsh, D. R., Neale, R. B., Rasch, P., Vavrus, S., Vertenstein, M., Bader, D., Collins, W. D., Hack, J. J., Kiehl, J., and Marshall, S.: The Community Earth System Model: A Framework for Collaborative Research, *Bulletin of the American Meteorological Society*, 94, 1339 – 1360, <https://doi.org/10.1175/BAMS-D-12-00121.1>, 2013.
- 585 Ivanovic, R. F., Gregoire, L. J., Kageyama, M., Roche, D. M., Valdes, P. J., Burke, A., Drummond, R., Peltier, W. R., and Tarasov, L.: Transient climate simulations of the deglaciation 21-9 thousand years before present (version 1) - PMIP4 Core experiment design and boundary conditions, *Geoscientific Model Development*, 9, 2563–2587, <https://doi.org/10.5194/gmd-9-2563-2016>, 2016.
- Kageyama, M., Albani, S., Braconnot, P., Harrison, S. P., Hopcroft, P. O., Ivanovic, R. F., Lambert, F., Marti, O., Peltier, W. R., Peterschmitt, J. Y., Roche, D. M., Tarasov, L., Zhang, X., Brady, E. C., Haywood, A. M., LeGrande, A. N., Lunt, D. J., Mahowald, N. M., Mikolajewicz, U., Nisancioglu, K. H., Otto-Bliesner, B. L., Renssen, H., Tomas, R. A., Zhang, Q., Abe-Ouchi, A., Bartlein, P. J., Cao, J., Li, Q., Lohmann, G., Ohgaito, R., Shi, X., Volodin, E., Yoshida, K., and Zheng, W.: The PMIP4 contribution to CMIP6 – Part 4: Scientific objectives and experimental design of the PMIP4-CMIP6 Last Glacial Maximum experiments and PMIP4 sensitivity experiments, *Geosci. Model Dev.*, 10, 4035–4055, <https://doi.org/10.5194/gmd-10-4035-2017>, gMD, 2017.
- 595 Kageyama, M., Harrison, S. P., Kapsch, M. L., Lofverstrom, M., Lora, J. M., Mikolajewicz, U., Sherriff-Tadano, S., Vadsaria, T., Abe-Ouchi, A., Bouttes, N., Chandan, D., Gregoire, L. J., Ivanovic, R. F., Izumi, K., Legrande, A. N., Lhardy, F., Lohmann, G., Morozova, P. A.,

- Ohgaito, R., Paul, A., Peltier, W. R., Poulsen, C. J., Quiquet, A., Roche, D. M., Shi, X., Tierney, J. E., Valdes, P. J., Volodin, E., and Zhu, J.: The PMIP4 Last Glacial Maximum experiments: Preliminary results and comparison with the PMIP3 simulations, *Climate of the Past*, 17, 1065–1089, <https://doi.org/10.5194/cp-17-1065-2021>, 2021.
- 600 Kaplan, J. O., Bigelow, N. H., Prentice, I. C., Harrison, S. P., Bartlein, P. J., Christensen, T. R., Cramer, W., Matveyeva, N. V., McGuire, A. D., Murray, D. F., Razzhivin, V. Y., Smith, B., Walker, D. A., Anderson, P. M., Andreev, A. A., Brubaker, L. B., Edwards, M. E., and Lozhkin, A. V.: Climate change and Arctic ecosystems: 2. Modeling, paleodata-model comparisons, and future projections, *Journal of Geophysical Research: Atmospheres*, 108, <https://doi.org/https://doi.org/10.1029/2002JD002559>, 2003.
- Kapsch, M.-L., Mikolajewicz, U., Ziemen, F. A., Rodehacke, C. B., and Schannwell, C.: Analysis of the surface mass balance for deglacial
605 climate simulations, *The Cryosphere*, 15, 1131–1156, <https://doi.org/10.5194/tc-15-1131-2021>, 2021.
- Kapsch, M.-L., Mikolajewicz, U., Ziemen, F., and Schannwell, C.: Ocean Response in Transient Simulations of the Last Deglaciation Dominated by Underlying Ice-Sheet Reconstruction and Method of Meltwater Distribution, *Geophysical Research Letters*, 49, e2021GL096767, <https://doi.org/https://doi.org/10.1029/2021GL096767>, <https://doi.org/10.1029/2021GL096767>, 2022.
- Klockmann, M., Mikolajewicz, U., and Marotzke, J.: American Meteorological Society Two AMOC States in Response to Decreasing Greenhouse Gas Concentrations in the Coupled Climate Model MPI-ESM, Source: *Journal of Climate*, 31, 7969–7984,
610 <https://doi.org/10.2307/26496703>, 2018.
- Lawrence, D. M., Fisher, R. A., Koven, C. D., Oleson, K. W., Swenson, S. C., Bonan, G., Collier, N., Ghimire, B., van Kampenhout, L., Kennedy, D., Kluzek, E., Lawrence, P. J., Li, F., Li, H., Lombardozzi, D., Riley, W. J., Sacks, W. J., Shi, M., Vertenstein, M., Wieder, W. R., Xu, C., Ali, A. A., Badger, A. M., Bisht, G., van den Broeke, M., Brunke, M. A., Burns, S. P., Buzan, J., Clark, M., Craig, A.,
615 Dahlin, K., Drewniak, B., Fisher, J. B., Flanner, M., Fox, A. M., Gentine, P., Hoffman, F., Keppel-Aleks, G., Knox, R., Kumar, S., Lenaerts, J., Leung, L. R., Lipscomb, W. H., Lu, Y., Pandey, A., Pelletier, J. D., Perket, J., Randerson, J. T., Ricciuto, D. M., Sanderson, B. M., Slater, A., Subin, Z. M., Tang, J., Thomas, R. Q., Val Martin, M., and Zeng, X.: The Community Land Model Version 5: Description of New Features, Benchmarking, and Impact of Forcing Uncertainty, *Journal of Advances in Modeling Earth Systems*, 11, 4245–4287, <https://doi.org/https://doi.org/10.1029/2018MS001583>, 2019.
- 620 Lecavalier, B. S., Milne, G. A., Simpson, M. J. R., Wake, L., Huybrechts, P., Tarasov, L., Kjeldsen, K. K., Funder, S., Long, A. J., Woodroffe, S., Dyke, A. S., and Larsen, N. K.: A model of Greenland ice sheet deglaciation constrained by observations of relative sea level and ice extent, *Quaternary Science Reviews*, 102, 54–84, <https://doi.org/https://doi.org/10.1016/j.quascirev.2014.07.018>, 2014.
- Lenaerts, J. T. M., Medley, B., van den Broeke, M. R., and Wouters, B.: Observing and Modeling Ice Sheet Surface Mass Balance, *Reviews of Geophysics*, 57, 376–420, <https://doi.org/https://doi.org/10.1029/2018RG000622>, 2019.
- 625 Lipscomb, W. H., Price, S. F., Hoffman, M. J., Leguy, G. R., Bennett, A. R., Bradley, S. L., Evans, K. J., Fyke, J. G., Kennedy, J. H., Perego, M., Ranken, D. M., Sacks, W. J., Salinger, A. G., Vargo, L. J., and Worley, P. H.: Description and evaluation of the Community Ice Sheet Model (CISM) v2.1, *Geoscientific Model Development*, 12, 387–424, <https://doi.org/10.5194/gmd-12-387-2019>, 2019.
- Liu, Z., Bao, Y., Thompson, L. G., Mosley-Thompson, E., Tabor, C., Zhang, G. J., Yan, M., Lofverstrom, M., Montanez, I., and Oster, J.: Tropical mountain ice core $\delta^{18}O$: A Goldilocks indicator for global temperature change, *Science Advances*, 9, eadi6725, <https://doi.org/10.1126/sciadv.adi6725>, 2023.
- 630 Lofverstrom, M., Fyke, J., Thayer-Calder, K., Muntjewerf, L., Vizcaino, M., Sacks, W. J., Lipscomb, W. H., Otto-Bliesner, B., and Bradley, S. L.: An efficient ice-sheet/Earth system model spin-up procedure for CESM2.1 and CISM2.1: description, evaluation, and broader applicability, *Journal of Advances in Modeling Earth Systems*, 12, e2019MS001984, <https://doi.org/10.1029/2019MS001984>, 2020.

- Lofverstrom, M., Thompson, D. M., Otto-Bliesner, B. L., and Brady, E. C.: The importance of Canadian Arctic Archipelago gateways for glacial expansion in Scandinavia, *Nature Geoscience*, 15, 482–488, <https://doi.org/10.1038/s41561-022-00956-9>, 2022.
- Loulergue, L., Schilt, A., Spahni, R., Masson-Delmotte, V., Blunier, T., Lemieux, B., Barnola, J.-M., Raynaud, D., Stocker, T. F., and Chappellaz, J.: Orbital and millennial-scale features of atmospheric CH₄ over the past 800,000 years, *Nature*, 453, 383–386, <https://doi.org/10.1038/nature06950>, 2008.
- Mix, A. C., Bard, E., and Schneider, R.: Environmental processes of the ice age: land, oceans, glaciers (EPILOG), *Quaternary Science Reviews*, 20, 627–657, [https://doi.org/https://doi.org/10.1016/S0277-3791\(00\)00145-1](https://doi.org/https://doi.org/10.1016/S0277-3791(00)00145-1), 2001.
- Mottram, R., Hansen, N., Kittel, C., van Wessem, J. M., Agosta, C., Amory, C., Boberg, F., van de Berg, W. J., Fettweis, X., Gossart, A., van Lipzig, N. P. M., van Meijgaard, E., Orr, A., Phillips, T., Webster, S., Simonsen, S. B., and Souverijns, N.: What is the surface mass balance of Antarctica? An intercomparison of regional climate model estimates, *The Cryosphere*, 15, 3751–3784, <https://doi.org/10.5194/tc-15-3751-2021>, 2021.
- Muglia, J. and Schmittner, A.: Carbon isotope constraints on glacial Atlantic meridional overturning: Strength vs depth, *Quaternary Science Reviews*, 257, 106 844, <https://doi.org/https://doi.org/10.1016/j.quascirev.2021.106844>, 2021.
- Muntjewerf, L., Petrini, M., Vizcaino, M., da Silva, C. E., Sellevold, R., Scherrenberg, M. D., Thayer-Calder, K., Bradley, S. L., Lenaerts, J. T., Lipscomb, W. H., and Lofverstrom, M.: Greenland Ice Sheet Contribution to 21st Century Sea Level Rise as Simulated by the Coupled CESM2.1-CISM2.1, *Geophysical Research Letters*, 47, <https://doi.org/10.1029/2019GL086836>, 2020a.
- Muntjewerf, L., Sellevold, R., Vizcaino, M., da Silva, C. E., Petrini, M., Thayer-Calder, K., Scherrenberg, M. D., Bradley, S. L., Katsman, C. A., Fyke, J., Lipscomb, W. H., Lofverstrom, M., and Sacks, W. J.: Accelerated Greenland Ice Sheet Mass Loss Under High Greenhouse Gas Forcing as Simulated by the Coupled CESM2.1-CISM2.1, *Journal of Advances in Modeling Earth Systems*, 12, <https://doi.org/10.1029/2019MS002031>, 2020b.
- Muntjewerf, L., Sacks, W. J., Lofverstrom, M., Fyke, J., Lipscomb, W. H., Ernani da Silva, C., Vizcaino, M., Thayer-Calder, K., Lenaerts, J. T. M., and Sellevold, R.: Description and Demonstration of the Coupled Community Earth System Model v2 – Community Ice Sheet Model v2 (CESM2-CISM2), *Journal of Advances in Modeling Earth Systems*, 13, e2020MS002 356, 2021.
- Noël, B., van de Berg, W. J., van Wessem, J. M., van Meijgaard, E., van As, D., Lenaerts, J. T. M., Lhermitte, S., Kuipers Munneke, P., Smeets, C. J. P. P., van Ulf, L. H., van de Wal, R. S. W., and van den Broeke, M. R.: Modelling the climate and surface mass balance of polar ice sheets using RACMO2 – Part 1: Greenland (1958–2016), *The Cryosphere*, 12, 811–831, <https://doi.org/10.5194/tc-12-811-2018>, 2018.
- Noël, B., van Kampenhout, L., van de Berg, W. J., Lenaerts, J. T. M., Wouters, B., and van den Broeke, M. R.: Brief communication: CESM2 climate forcing (1950–2014) yields realistic Greenland ice sheet surface mass balance, *The Cryosphere*, 14, 1425–1435, <https://doi.org/10.5194/tc-14-1425-2020>, 2020.
- Oleson, K., Lawrence, D. M., Bonan, G. B., Drewniak, B., Huang, M., Koven, C. D., Levis, S., Li, F., Riley, W. J., Subin, Z. M., Swenson, S. C., Thornton, P. E., Bozbiyik, A., Fisher, R., Heald, C. L., Kluzek, E., Lamarque, J.-F., Lawrence, P. J., Leung, L. R., Lipscomb, W., Muszala, S., Ricciuto, D. M., Sacks, W., Sun, Y., Tang, J., and Yang, Z.-L.: Technical description of version 4.5 of the Community Land Model (CLM), NCAR Tech. Note NCAR/TN-503 + STR, 2013.
- Osman, M. B., Tierney, J. E., Zhu, J., Tardif, R., Hakim, G. J., King, J., and Poulsen, C. J.: Globally resolved surface temperatures since the Last Glacial Maximum, *Nature*, 599, 239–244, <https://doi.org/10.1038/s41586-021-03984-4>, 2021.

- 670 Patton, H., Hubbard, A., Andreassen, K., Winsborrow, M., and Stroeven, A. P.: The build-up, configuration, and dynamical sensitivity of the Eurasian ice-sheet complex to Late Weichselian climatic and oceanic forcing, *Quaternary Science Reviews*, 153, 97–121, <https://doi.org/https://doi.org/10.1016/j.quascirev.2016.10.009>, 2016.
- Paul, A., Mulitza, S., Stein, R., and Werner, M.: A global climatology of the ocean surface during the Last Glacial Maximum mapped on a regular grid (GLOMAP), *Clim. Past*, 17, 805–824, <https://doi.org/10.5194/cp-17-805-2021>, cP, 2021.
- 675 Peltier, W. R.: GLOBAL GLACIAL ISOSTASY AND THE SURFACE OF THE ICE-AGE EARTH: The ICE-5G (VM2) Model and GRACE, *Annual Review of Earth and Planetary Sciences*, 32, 111–149, <https://doi.org/10.1146/annurev.earth.32.082503.144359>, doi: 10.1146/annurev.earth.32.082503.144359, 2004.
- Peltier, W. R., F., A. D., and R., D.: Space geodesy constrains ice age terminal deglaciation: The global ICE-6G_C (VM5a) model, *Journal of Geophysical Research: Solid Earth*, 120, 450–487, <https://doi.org/https://doi.org/10.1002/2014JB011176>, 2015.
- 680 Petit, J. R., Jouzel, J., Raynaud, D., Barkov, N. I., Barnola, J. M., Basile, I., Bender, M., Chappellaz, J., Davis, M., Delaygue, G., Delmotte, M., Kotlyakov, V. M., Legrand, M., Lipenkov, V. Y., Lorius, C., Pépin, L., Ritz, C., Saltzman, E., and Stievenard, M.: Climate and atmospheric history of the past 420,000 years from the Vostok ice core, Antarctica, *Nature*, 399, 429–436, <https://doi.org/10.1038/20859>, 1999.
- Quiquet, A., Roche, D. M., Dumas, C., Bouttes, N., and Lhardy, F.: Climate and ice sheet evolutions from the last glacial maximum to the pre-industrial period with an ice-sheet–climate coupled model, *Clim. Past*, 17, 2179–2199, <https://doi.org/10.5194/cp-17-2179-2021>, cP, 2021.
- 685 Schilt, A., Baumgartner, M., Schwander, J., Buiron, D., Capron, E., Chappellaz, J., Loulergue, L., Schüpbach, S., Spahni, R., Fischer, H., and Stocker, T. F.: Atmospheric nitrous oxide during the last 140,000 years, *Earth and Planetary Science Letters*, 300, 33–43, <https://doi.org/https://doi.org/10.1016/j.epsl.2010.09.027>, 2010.
- 690 Sellevold, R. and Vizcaíno, M.: Global Warming Threshold and Mechanisms for Accelerated Greenland Ice Sheet Surface Mass Loss, *Journal of Advances in Modeling Earth Systems*, 12, <https://doi.org/10.1029/2019MS002029>, 2020.
- Sellevold, R. and Vizcaíno, M.: Global Warming Threshold and Mechanisms for Accelerated Greenland Ice Sheet Surface Mass Loss, *Journal of Advances in Modeling Earth Systems*, 12, e2019MS002029, <https://doi.org/https://doi.org/10.1029/2019MS002029>, e2019MS002029 10.1029/2019MS002029, 2020.
- 695 Sellevold, R., Kampenhout, L. V., Lenaerts, J. T., Noël, B., Lipscomb, W. H., and Vizcaino, M.: Surface mass balance downscaling through elevation classes in an Earth system model: Application to the Greenland ice sheet, *Cryosphere*, 13, 3193–3208, <https://doi.org/10.5194/tc-13-3193-2019>, 2019.
- Sherriff-Tadano, S. and Abe-Ouchi, A.: Roles of Sea Ice–Surface Wind Feedback in Maintaining the Glacial Atlantic Meridional Overturning Circulation and Climate, *Journal of Climate*, 33, 3001–3018, <https://doi.org/10.1175/JCLI-D-19-0431.1>, 2020.
- 700 Sherriff-Tadano, S., Abe-Ouchi, A., Yoshimori, M., Oka, A., and Chan, W.-L.: Influence of glacial ice sheets on the Atlantic meridional overturning circulation through surface wind change, *Climate Dynamics*, 50, 2881–2903, <https://doi.org/10.1007/s00382-017-3780-0>, 2018.
- Smith, R. S., Mathiot, P., Siahahan, A., Lee, V., Cornford, S. L., Gregory, J. M., Payne, A. J., Jenkins, A., Holland, P. R., Ridley, J. K., and Jones, C. G.: Coupling the U.K. Earth System Model to Dynamic Models of the Greenland and Antarctic Ice Sheets, *Journal of Advances in Modeling Earth Systems*, 13, e2021MS002520, <https://doi.org/https://doi.org/10.1029/2021MS002520>, e2021MS002520 2021MS002520, 2021.
- 705

- Sommers, A. N., L., O.-B. B., H., L. W., Marcus, L., L., S. S., J., B. P., C., B. E., Erik, K., Gunter, L., Katherine, T.-C., and A., T. R.: Retreat and Regrowth of the Greenland Ice Sheet During the Last Interglacial as Simulated by the CESM2-CISM2 Coupled Climate–Ice Sheet Model, *Paleoceanography and Paleoclimatology*, 36, e2021PA004272, <https://doi.org/https://doi.org/10.1029/2021PA004272>, e2021PA004272 2021PA004272, 2021.
- 710
- Sun, Q., Michael, M. W., Bryan, F. O., and heng Tseng, Y.: A box model for representing estuarine physical processes in Earth system models, *Ocean Modelling*, 112, 139–153, <https://doi.org/https://doi.org/10.1016/j.ocemod.2017.03.004>, 2017.
- Tarasov, L., Dyke, A. S., Neal, R. M., and Peltier, W. R.: A data-calibrated distribution of deglacial chronologies for the North American ice complex from glaciological modeling, *Earth and Planetary Science Letters*, 315-316, 30–40, 715 <https://doi.org/https://doi.org/10.1016/j.epsl.2011.09.010>, 2012.
- Tierney, J. E., Zhu, J., King, J., Malevich, S. B., Hakim, G. J., and Poulsen, C. J.: Glacial cooling and climate sensitivity revisited, *Nature*, 584, 569–573, <https://doi.org/10.1038/s41586-020-2617-x>, 2020.
- van den Broeke, M., Smeets, P., Ettema, J., van der Veen, C., van de Wal, R., and Oerlemans, J.: Partitioning of melt energy and meltwater fluxes in the ablation zone of the west Greenland ice sheet, *The Cryosphere*, 2, 179–189, <https://doi.org/10.5194/tc-2-179-2008>, 2008.
- 720 van Kampenhout, L., Lenaerts, J. T. M., Lipscomb, W. H., Sacks, W. J., Lawrence, D. M., Slater, A. G., and van den Broeke, M. R.: Improving the Representation of Polar Snow and Firn in the Community Earth System Model, *Journal of Advances in Modeling Earth Systems*, 9, 2583–2600, <https://doi.org/https://doi.org/10.1002/2017MS000988>, 2017.
- van Kampenhout, L., Lenaerts, J. T. M., Lipscomb, W. H., Lhermitte, S., Noël, B., Vizcaíno, M., Sacks, W. J., and van den Broeke, M. R.: Present-Day Greenland Ice Sheet Climate and Surface Mass Balance in CESM2, *Journal of Geophysical Research: Earth Surface*, 125, 725 e2019JF005318, <https://doi.org/https://doi.org/10.1029/2019JF005318>, 2020.
- van Kampenhout, L., Lenaerts, J. T. M., Lipscomb, W. H., Lhermitte, S., Noël, B., Vizcaíno, M., Sacks, W. J., and van den Broeke, M. R.: Present-Day Greenland Ice Sheet Climate and Surface Mass Balance in CESM2, *Journal of Geophysical Research: Earth Surface*, 125, e2019JF005318, <https://doi.org/https://doi.org/10.1029/2019JF005318>, e2019JF005318 10.1029/2019JF005318, 2020.
- Vizcaíno, M., Lipscomb, W. H., Sacks, W. J., van Angelen, J. H., Wouters, B., and van den Broeke, M. R.: Greenland Surface Mass Balance as 730 Simulated by the Community Earth System Model. Part I: Model Evaluation and 1850–2005 Results, *Journal of Climate*, 26, 7793–7812, <https://doi.org/10.1175/JCLI-D-12-00615.1>, 2013.
- Whitehouse, P. L.: Glacial isostatic adjustment modelling: historical perspectives, recent advances, and future directions, *Earth Surf. Dynam.*, 6, 401–429, <https://doi.org/10.5194/esurf-6-401-2018>, eSurf, 2018.
- Zhu, J., Liu, Z., Zhang, X., Eisenman, I., and Liu, W.: Linear weakening of the AMOC in response to receding glacial ice sheets in CCSM3, 735 *Geophysical Research Letters*, 41, 6252–6258, 2014.
- Zhu, J., Otto-Bliesner, B. L., Brady, E. C., Poulsen, C. J., Tierney, J. E., Lofverstrom, M., and DiNezio, P.: Assessment of Equilibrium Climate Sensitivity of the Community Earth System Model Version 2 Through Simulation of the Last Glacial Maximum, *Geophysical Research Letters*, 48, e2020GL091220, <https://doi.org/https://doi.org/10.1029/2020GL091220>, e2020GL091220 2020GL091220, 2021.
- Zhu, J., Otto-Bliesner, B. L., Brady, E. C., Gettelman, A., Bacmeister, J. T., Neale, R. B., Poulsen, C. J., Shaw, J. K., McGraw, Z. S., and Kay, 740 J. E.: LGM paleoclimate constraints inform cloud parameterizations and equilibrium climate sensitivity in CESM2, *Journal of Advances in Modeling Earth Systems*, 14, e2021MS002776, 2022.
- Ziemen, F. A., Rodehacke, C. B., and Mikolajewicz, U.: Coupled ice sheet–climate modeling under glacial and pre-industrial boundary conditions, *Clim. Past*, 10, 1817–1836, <https://doi.org/10.5194/cp-10-1817-2014>, cP, 2014.